TURBULENCE MEASUREMENTS IN A FAN-STIRRED FLAME BOMB USING LASER DOPPLER VELOCIMETRY

A Thesis

by

ANÍBAL MORONES RUELAS

Submitted to the Office of Graduate and Professional Studies of
Texas A&M University
in partial fulfillment of the requirements for the degree of

MASTER OF SCIENCE

Chair of Committee,	Eric L. Petersen
Committee Members,	Gerald L. Morrison
	Adonios N. Karpetis
Head of Department,	Andreas A. Polycarpou

August 2015

Major Subject: Mechanical Engineering

ABSTRACT

An ongoing project for the construction of a high-pressure, high-temperature turbulent flame speed vessel is furthered in this study. Prior to this work, a laminar flame bomb apparatus was repurposed as a turbulent flame speed vessel with the addition of four fans. Several impeller prototypes were proposed and tested in a mock model. The turbulence was characterized with PIV. At that time, homogenous and isotropic flow field and negligible mean flow were found at the plane of measurement, but the study was limited to a small area and one fan speed.

The turbulence characterization is revisited here with a newly acquired LDV system. The study objectives are to: confirm the PIV measurements with LDV, this time in the actual vessel; expand the interrogation area from a plane to a 3d volume; asses the performance of the impellers at different levels rotational speed, and; provide a more direct assessment of the temporal scale.

Basic concepts on the statistical description of turbulence were introduced. The LDV principle of operation and the function of the elements comprising the LDV system were explained.

The method developed for the experimentation was presented along with all the relevant parameters and adjustments in the control of the experiment. Two levels of fan speed were chosen to run in the modified turbulent vessel, namely 8,000 and 12,000 rpm. A

tridimensional space situated at the center of the vessel was systematically scanned and turbulence statistics were obtained.

The results confirmed some of the observations of the PIV, but the extension of the measurements to a tridimensional region also revealed unfavorable characteristics previously missed.

The work concludes suggesting improvements for a new design of turbulent flame bomb. In particular a new arrangement of the fans is advised.

To my family.

ACKNOWLEDGMENTS

First I want to thank my advisor and committee chair, Dr. Eric L. Petersen. I must express my deepest gratitude for his support, mentorship and patience. I honed skills during my stay in his laboratory that has made me a more useful element to society.

I also would like to thank my committee members, Dr. Morrison and Dr. Karpetis for their counsel and discussions that helped this newcomer into the laser diagnostic techniques to find his way.

I will not attempt to list all names of my peers at the Petersen research group, with whom I shared many experiences, travels and challenges. I will say, though, that in their company I felt inspired, motivated, and fortunate.

Finally, thanks to my sidekick and navigator in this overseas graduate adventure: my lovely wife Liliana Yadira. She has taught me that home is not a place. Home is in her arms.

NOMENCLATURE

AOA Angle of Attack

FOV Field of View

HIT Homogeneous Isotropic Turbulence

LED Light Emitting Diode

LDV Laser Doppler Velocimetry

mW milliWatt ($W \times 10^{-3}$)

OPR once-per-rev

PMT Photomultiplier Tube

RMS Root Mean Square

VAC Volts Alternating Current

TABLE OF CONTENTS

Page

LIST OF FIGURES

Page

LIST OF TABLES

Page

1. INTRODUCTION

The present work is part of a continuing effort to develop a high-pressure, high-temperature bomb for spherically expanding turbulent flame speed experiments at Texas A&M University. Previously, an existing aluminum laminar flame speed bomb, Figure 1, was repurposed for turbulent experiments by retrofitting a set of four (4) fans to generate turbulence, Figure 2.

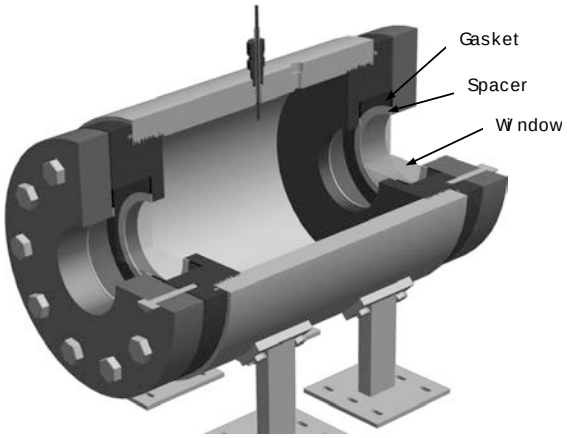

Figure 1 Original laminar flame speed aluminum bomb. Reproduced from [1].

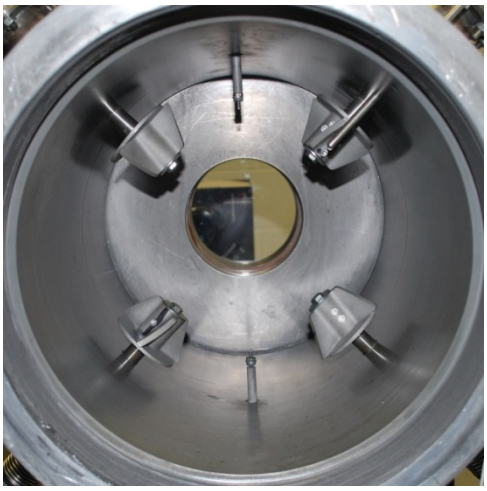

Figure 2 Interior of vessel showing the impellers. One endcap was removed to take the picture.

The impellers for the current vessel were designed in house [2, 3]. Three (3) prototypes were tested in a transparent mock up vessel model using Particle Image Velocimetry, PIV, as seen in Figure 3. The flow inside the model showed a good degree of homogeneity and isotropy, while the ratio of average velocity to the turbulence fluctuation rms was acceptable. The integral length scale was measured with spatial

correlations. Moreover, control over the integral length scale was demonstrated by changing the impeller geometry as other groups have reported for fan stirred vessels [4-7].

However, the characterization suffered from the following shortcomings:

1. Only one level of fan speed was tested: 8300 ±100 rpm. Therefore the dependence of turbulence intensity on fan speed could not be verified.
2. The measurements were limited to one plane at the middle of the vessel that contained the four (4) fan axes.
3. The field of view, FOV, was relatively small: approximately 36×26 mm^2. The FOV was not large enough to find the end of spatial coherence in the space correlation [8].
4. No confirmation from a technique other than PIV was available.
5. The Plexiglas model had roughly the same interior dimensions as the aluminum bomb it meant to represent, but it was stripped of detailed features. It was assumed the features not reproduced had little effect in the flow field.

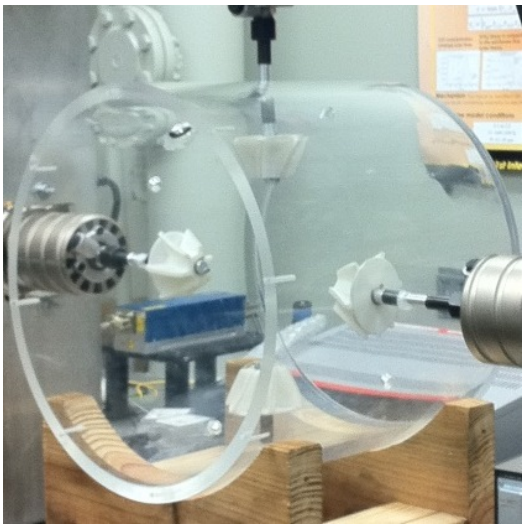

Figure 3 Plexiglas model at 1:1 scale. Six (6) bladed prototype impellers are installed.

Five objectives were defined to further the greater goal of a new purposely built turbulent vessel. The objectives of this study are to:

1. Confirm the PIV measurements with LDV.
2. Confirm the flow field established in the mock model was true to the actual aluminum vessel.
3. Expand the interrogation area from a plane to a 3d volume.
4. Measure more levels of fan speed.
5. Provide a more direct assessment of the temporal scale.

This manuscript is structured in sections. First some basic concepts on the statistical description of turbulence are introduced. The use of autocorrelations for the extraction of time scales in turbulence is also explained. The text ensues with the details of the experimental setup. The LDV principle of operation is illustrated and the elements comprising the concrete LDV system that facilitated this study are specified. The method developed for the preparation of the optics in the experiment is presented step by step. All the relevant parameters and adjustments in the control of the experiment are summarized in a subsection titled “Experimental Settings” followed by the disclosure of the experimental plan. The results and their discussion are integrated in one section. Finally, conclusions are drawn and recommendations for the new vessel design are made.

2. TURBULENCE DESCRIPTION

2.1. Characteristics of turbulence

Turbulence is a state of flow that might seem totally random at first glance. However, a closer inspection may find some degree of motion coherence in time and in space. A red laser line and oil fog in Figure 4 reveal patches of coherent flow. These regions of coherence are called eddies. A whole collection of eddies of different sizes coexist in the flow. The biggest of eddies usually have characteristic dimensions comparable to the system, in this case, the vessel diameter. Turbulent structures are inherently tridimensional, not steady and, in general, complex to describe. Homogenous and isotropic turbulence, HIT, one of the simplest cases because the turbulence has statistically no preference in direction and the kinetic energy in the eddies, is uniformly distributed in space.

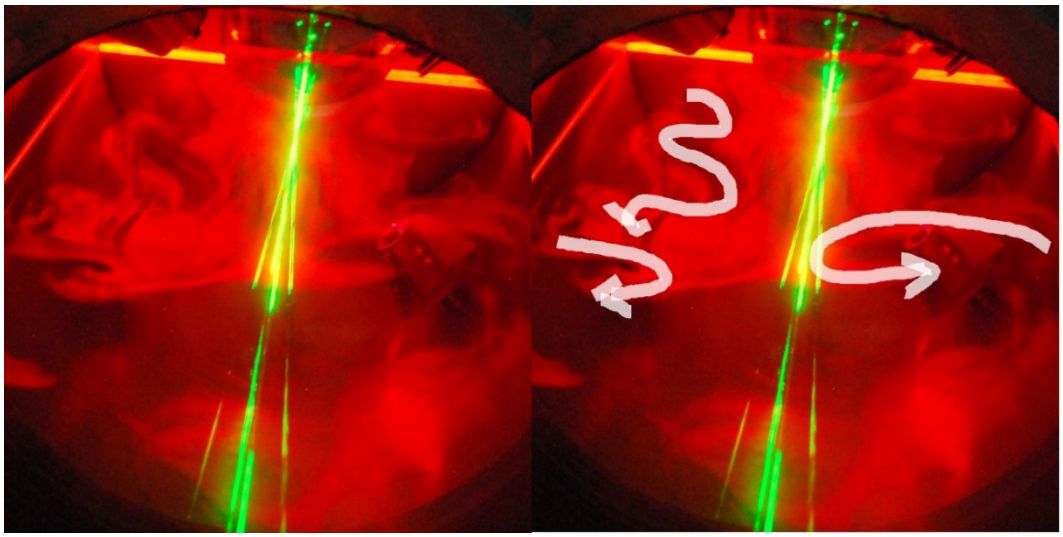

Figure 4 Patterns of motion in the mist are revealed by the red laser line inside the aluminum bomb. The green laser beams belong to the LDV system described in the next section.

HIT with no mean flow is the state that all spherically expanding turbulent flame bombs aim to create [6-16].

Some of the trademark characteristics of turbulence are [17]:

1. Fluctuations: Turbulence exhibits fluctuations that cannot be predicted in detail deterministically or with statistical analysis.
2. Nonlinearity: Turbulence is triggered when a critical ratio of inertial to viscous forces is exceeded. For low Reynolds numbers, the flow regime is not chaotic. In laminar flow, small disturbances are dissipated without destroying the streamlines of the flow. However as the inertial forces increase, a threshold is trespassed, and disturbances grow and propagate, defacing ordered flow.
3. Vorticity: The motion in turbulent flows is very complex, and all kinds of effects are present, strain, stretch, deform and so on, but the signature of turbulence is the spinning structures, or eddies.
4. Dissipation: Turbulence dissipates kinetic energy into heat by the effects of viscosity. A turbulent flow will eventually cease if not supported by an input of kinetic energy.
5. Diffusivity: Turbulence potentiates the rate of mixing in the flow. Momentum, species and heat diffusion are augmented in turbulent flow compared to laminar flow.

2.2. Statistical description of turbulence

It is customary to describe turbulence to approach the solution of the fluid dynamics of turbulence by decomposing it into the first moment and fluctuations. An arbitrary dependent field variable $\tilde{a}(t;\mathbf{x})$ (e.g. velocity components, pressure, temperature, etc.) can be split in two parts, eq. (1)

$$\tilde{a}(t;\mathbf{x}) = A(\mathbf{x}) + a(t;\mathbf{x}) \tag{1}$$

Where:

$A(\mathbf{x})$	First moment of the dependent field variable, (mean of $\tilde{a}(t;\mathbf{x})$)
$a(t;\mathbf{x})$	Fluctuations of the dependent field variable (zero mean by definition)
$\mathbf{x}$	Spatial location (x,y,z)
t	Time

Figure 5 provides an example of the decomposition of an arbitrary variable. The blue line is the instantaneous value as a function of time, $\tilde{a}(t;\mathbf{x})$. The red dotted line is the average or first moment over the period τ, $A(\mathbf{x}) = 1/\tau \int^{\tau} \tilde{a}(t,\mathbf{x})\, dt$. Notice that at any time, the arbitrary variable can be described as the sum of the average value and the fluctuation.

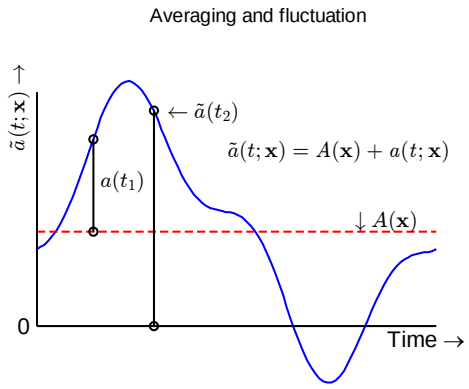

Figure 5 Decomposition of speed in first moment and fluctuation.

Strictly speaking, the temporal averaging of any dependent field variable is a function of the period length. Consider, for example, that only the velocity in the period between t_1 and t_2 had been used in the figure above. The resultant average would have been higher than the overall average marked by the red dotted line. A flow is said to be stationary when the statistics of the flow do not depend on time and on the limit converge to a value. It can be inferred that a minimum meaningful period must be encompassed.

2.3. Spatial and time correlations

Previous subsections have suggested the existence of meaningful temporal and spatial scales in the turbulent flow, e.g. the size of the eddies and the time periods for temporal averaging. These scales are valuable to characterize turbulence. They describe the extent in time and space turbulence coherence.

Autocorrelations are a way to quantify the temporal coherence in a turbulent flow. Let $a(t;\mathbf{x})$ be the fluctuation of an arbitrary field variable. The temporal coefficient of correlation, $r(\tau,\mathbf{x})$, of $a(t;\mathbf{x})$ for time shift τ is defined in eq. (2). Notice that if $\tau = 0$ the coefficient of correlation becomes unity since $\overline{a(t;\mathbf{x})a(t+0;\mathbf{x})} = \overline{a^2(\mathbf{x})}$. It is expected that the coefficient of temporal correlation will drop as the time shift increases and eventually becomes zero when the $a(t;\mathbf{x})$ becomes uncorrelated with itself.

$$r(\tau;\mathbf{x}) = \frac{\overline{a(t;\mathbf{x})a(t+\tau;\mathbf{x})}}{\overline{a^2(\mathbf{x})}} \tag{2}$$

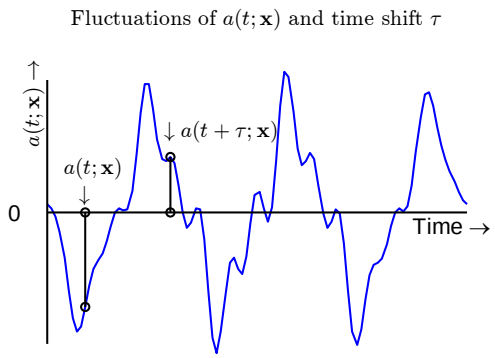

Figure 6 The time series of $a(t;\mathbf{x})$ and $a(t+\tau;\mathbf{x})$). The starting points of both series are indicated.

The temporal coefficient of correlation cannot be directly obtained for variables that are not sampled at even time steps, as is the case of LDV. Since the arrival time of particles is random, the LDV system acquires readings essentially whenever available. A "slotted" approach is a common tool to deal with LDV temporal correlation [18, 19].The slotted method categorizes the readings' time stamps in bins that are regularly spaced and then computes the correlation coefficient.

3. EXPERIMENTAL SETUP

3.1. Laser Doppler Velocimetry

The LDV is a technique that allows the measurement of the velocity of particles. Two laser beams are focused and crossed at a point where the velocity magnitude is wanted, see Figure 7. The laser beams have the same wavelength, and their intersection creates a volume of interference also known as the probe volume. A uniformly spaced fringe pattern is produced as a result of the constructive and destructive interference between the beams. The fringes are bright and dark planes that alternate and divide the probe volume in slices, shown as horizontal bands at the center of Figure 7. Bright slices are planes of constructive interference, and dark slices are planes of destructive interference.

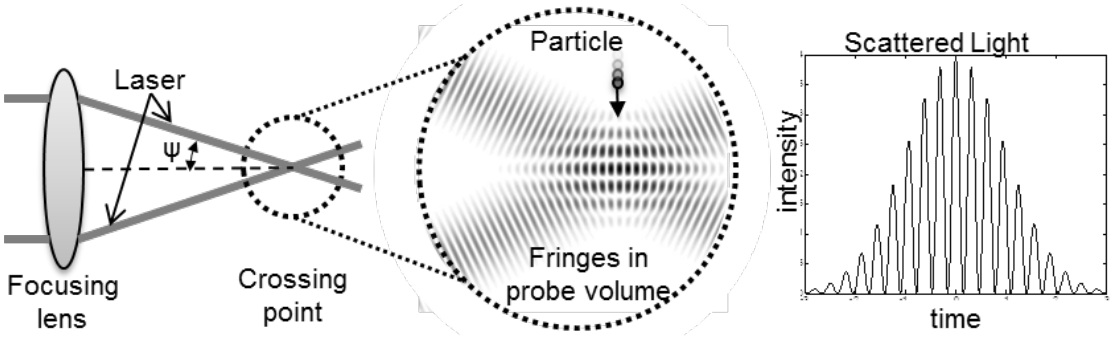

Figure 7 A particle traversing the probe volume scatters light. The frequency in the fluctuations of the scattered light intensity is proportional to the particle speed. The fringe pattern is horizontal in this representation. Fringe pattern modified from http://commons.wikimedia.org/wiki/File:Interferences_plane_waves.jpg

The distance between the fringes is a function of the half angle between the beams and the laser wavelength as it is shown in eq. (3) [20]. A particle traversing the probe volume will scatter light that fluctuates in intensity as the particle moves through bright and dark

slices of the probe volume. A sample scattering burst is shown on right side of Figure 7. The intensity fluctuation frequency and the known fringe spacing can then be used to calculate the particle velocity with the help of eq. (4).

$$d_f = \frac{\lambda}{2Sin\psi} \tag{3}$$

$$u = d_f \, f_b \tag{4}$$

Where:

d_f	Fringe spacing
λ	Laser wavelength
ψ	Half angle
u	Particle velocity
f_b	Scattered light burst frequency

The fringe pattern created in the mechanism described above is static, in other words, the bright and dark planes' relative position does not move within the probe volume. This generates a problem because particles moving with the same speed but opposite sense (in same direction) are indistinguishable, since they produce identical scattering bursts. One way to solve this is to shift the frequency of one of the beams. This sets the fringes in motion within the probe volume. The velocity at which the fringes move is determined by the magnitude of the frequency shift. With the fringes in motion, a relative velocity now exists between the fringes and the particles. Particles moving in the same direction as the fringes will produce different signatures than those moving in the opposite sense

due to the Doppler Effect. A signal processor analyzes the burst frequency and relies on the known shift to differentiate the direction and the speed of the particles.

The particles, also known as seeds, may be already part of the flow under study or they may be added intentionally if the flow lacks suitable tracers. Seeds can be small solid particles or liquid droplets, but they must have some key characteristics [21]:

1. Scatter sufficient light to be detected
2. Truthfully follow the flow
3. Their number must be high enough to produce an acceptable data rate
4. Safe to handle
5. Survive the conditions in the flow
6. Reasonably inexpensive

The seeds used in laser velocimetry are much smaller than the probe volume waist, with a diameter comparable to the wavelength of the laser. The light scattered by this kind of particle is best described with Mie scattering.

An atomizer seed generator was used in this work to inject particles into the flow stream. In this kind of generator, seeds are produced from liquids, solutions, and suspensions with the help of a compressed air jet. Table 1 lists some of the particle properties for several liquid materials. For this work, olive oil was the material of choice because it is inexpensive and readily available.

Table 1 Properties of selected seed materials of the Model 9306 Six-Jet Atomizer. Reproduced from [21]

Material	Density	Refractive index	Vapor Pressure	Mean Particle Size (μm)	Particle output concentration (particles/cc)
Dioctyl Phthalate (DOP)	0.9861	1.49	1.2 mmHg @200C	<0.6	4.3×10^{6}
Polyethylene Glycol 400	1.11	1.45	Very low	≈0.6	1.2×10^{6}
Oleic Acid	0.895	1.46	10 mmHg @223C	<0.6	4.0×10^{6}
Olive Oil	0.913	1.47	Very low	<0.6	4.0×10^{6}
Propylene Glycol	1.04	1.43	760 mm @188C	≈0.6	2.0×10^{5}
Sugar Solution	1.58	1.54	-	Variable	1.0×10^{6}
Salt Solution	2.46	1.54	-	Variable	1.0×10^{6}
PSL	1.03-1.05	1.60	-	Variable	1.0×10^{4}

3.2. LDV system

A new TSI LDV system was used in this study. The system is composed of several devices listed in Table 2. The lasers and the receiving optics are conveniently integrated into one probe, greatly simplifying the setup compared to an individual laser source, transmitting optics and light collecting optics.

The probe has two solid state lasers, rated 300 mW each. The lasers wavelengths are 532 and 561 nm. These lasers are very convenient because they do not require water cooling and are powered with a 1 phase, low-tension voltage source, i.e. 120 VAC or 240 VAC. The probe volume standoff is set by the front lens focal length. Currently, two interchangeable front lens are available with focal lengths of 362.6 mm and 512.3 mm.

For this work, a 512.3-mm front lens was selected. The probe is mounted on an Isel brand 3-axis, heavy duty traverse system. The traverse is automated and has a range of 600x600x600 mm.

The light collected by the transceiver receiving optics and is sent via optical fiber to the PMT to be converted into an analog electrical signal. Then, the signal processor is in charge of identifying the bursts from the background noise and extracts their frequency.

The signal processor has been enhanced with an External Input Card (EIC) module. The EIC module extends the inputs that can be recorded along with the velocity data. The EIC adds four analog channels, four digital channels, plus one once-per-rev (OPR) signal. The OPR input channel can be used to coordinate the data acquisition of rotating machinery.

Table 2 LDV system components

Device	**Model**
Transceiver	PowerSight TR-SS-2D
Signal processor	FSA4000-2
Traverse	T3DH
Photomultiplier	PDM1000-2SS
Particle Generator	9306
Computer	Dell Precision T7600

3.3. Optics preparation

The LDV probe, the traverse system that moves the LDV, and the flame bomb have to be properly aligned and referenced to map the flow field accurately. The preparation starts by roughly leveling the ZX plane of the flame bomb and the traverse system, shown in green in Figure 8. A simple bubble level suffices for this task, since further steps will ensure a better alignment.

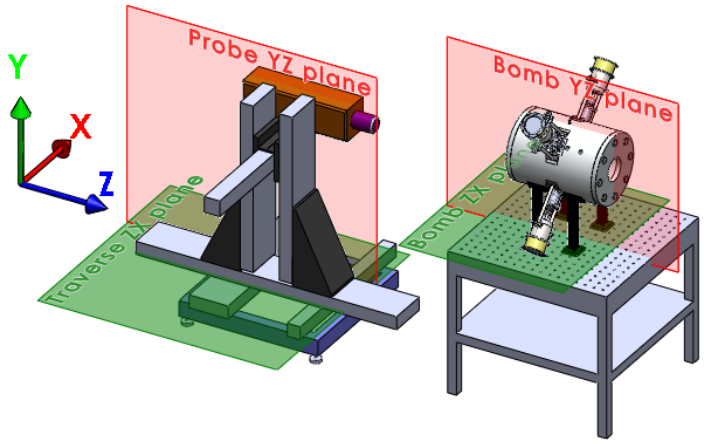

Figure 8 Experiment setup planes. ZX planes shown in green. YZ planes shown in red.

The next step is the alignment of traverse and bomb YZ planes, shown in red in Figure 8. A laser line serves as a guide for this task in Figure 9. The laser line was previously made plumb. It is important to choose a location that enables the alignment of the Z axis rail of the traverse, which is close to the floor and, at the same time, provides a vertical reference for the bomb and the Y axis rail.

Since the probe can rotate on its base, it must be independently verified even when the traversing and bomb YZ planes are parallel. Using the same laser line and pieces of

paper, the alignment of the LDV laser beams is performed. The center and right pictures in Figure 9 show that the LDV beams and the laser line are in the same plane.

The electrode bores serve as “viewfinder” and bull’s-eye to find the coordinate system origin. This is convenient because the electrode bores are located on opposite sides of the circumference, and the line of sight that joins them passes through the geometric center of the vessel, Figure 10.

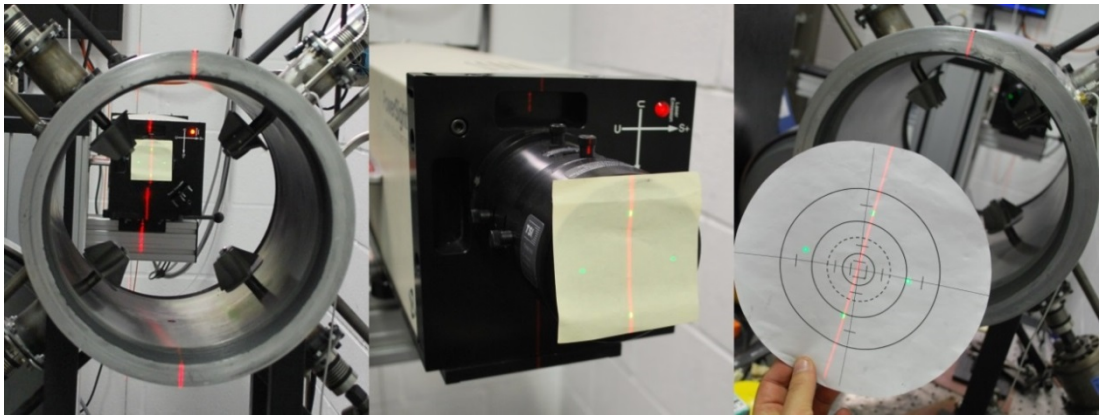

Figure 9 A red laser line is used to align the bomb, the traverse and the LDV. Paper pieces are useful to align the LDV beams and the laser line.

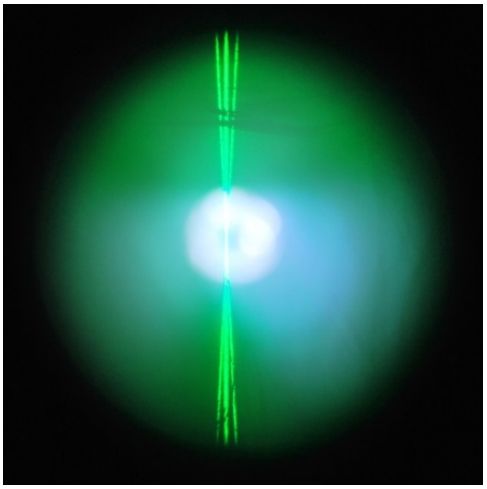

Figure 10 Probe volume seen through the electrode bore

The final step in the alignment is to rectify the ZX planes. This alignment is done with the vessel endcaps installed. One of the windows is covered with a paper template, and the location of the laser dots is noted. Then the other window is covered with the template, and the location of the laser dots should match.

The correct steering of the laser beams to the front lens focal point is critical. On one hand, the probe volume must be placed at the focal point of the receiving optics to maximize the amount of scattered light collection. On the other, the overlap of the 532-nm and 561-nm probe volumes is very important to obtain simultaneous readings of vertical and horizontal velocity. To achieve a proper probe volume positioning, the location of the focal point must be found. The focal point is made visible with the help of a red LED that temporary replace the photomultiplier sensor. The LED sends light through the receiving optics and focuses it at the focal point in front of the LDV probe. A 40X microscope objective is placed at the focal point and projects an amplified image on a screen, Figure 11. When the microscope objective is at the right location, a small red dot or circle appears. The red dot edge should be well defined. When the microscope objective is out of focus, the red dot becomes bigger and blurry. Once the focal point is found, all the laser beams are steered to this location. A laser beam that is properly steered will project a dot on the screen that overlaps with the LED dot. The centroids of the dots must be made coincident.

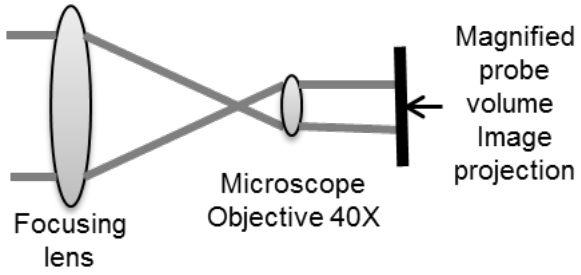

Figure 11 The probe volume is magnified with a 40X microscope objective.

Reflections are a concern in LDV setups because they can find their way back to the receiving optics and overwhelm the PMT, rendering it blind to the relatively miniscule probe volume scattered light intensity. So reflections should be blocked before they reach the receiving optics.

3.4. Experimental settings

The amount of data and their quality depend heavily on several parameters that are referred here collectively as experimental settings. Many are directly related to the LDV control itself. Table 3 summarizes the experimental settings in this work. On average, the data rate achieved was 4000 coincident measurements per second. Only readings that were deemed simultaneous by the coincidence parameters were considered valid data points.

Table 3 Experimental settings

Control parameter	Setting
PMT Voltage	600 V
Burst Threshold	180 mV
SNR	Low
Band Pass Filter	1-10 MHz
Downmix Freq.	34.5 MHz
Gate scale	250 %
Coincidence interval	1 μs
Atomizer	4 s@3 jets
Gatetime Weighting	Enabled
Fan run time	22 s

The Photomultiplier voltage sets the gain of the transformation between light intensity and the electrical signal. According to the manufacturer, the optimum voltage range will fall between 350 V and 600 V. The upper limit was set since a monotonic positive relation was found between the data rate and PMT voltage. Values higher than 600 V were found to saturate the PMT.

The manufacturer recommends a burst threshold between 30 mV and 300 mV if seed particles less than 10 μm are used. It was found that a threshold less than 180 mV produced very low burst efficiency, probably due false positive bursts. Moreover, since relatively high threshold was chosen, the signal to noise ratio was set to Low.

The band pass filter allows one to maximize the resolution of the sampler in the signal analyzer by focusing the processing capacity in the specified range of frequency. The width of the filter, combined with the downmix frequency determines the range of velocities that will be resolved by the signal processor. The downmix shifts the bursts frequency to a region that the band pass filter will let it through. A downmix frequency of 34.5 MHz combined with a band pass filter of 1- 10 MHz allows to measure velocities up to ±25.9m/s in the vertical direction and ± 25.56 in the horizontal direction. This range was found to be adequate for the magnitudes present in the stirred bomb, considering the standard deviation of the velocity is roughly 1.6 m/s in either direction, see the illustration in Figure 12. In other words, window of velocity that the downmixer and the filter will allow to pass is more 30 wider than the expected standard deviation.

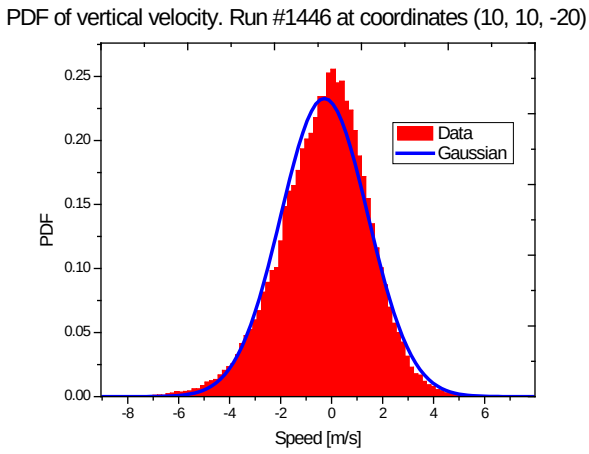

Figure 12 Speed histogram. The frequency has been normalized. Notice the resemblance with a Gaussian distribution.

If Reynolds stresses are desired, then the simultaneous measurement of the vertical and horizontal velocity is needed. Gate scale and coincidence interval set the limits for the

bursts that will be considered as coincident or simultaneous. The gate time is the duration of a scattered light burst. The burst gates are enlarged to find possible overlaps. The coincidence interval works in a similar way, but it is defined as a constant window of time instead of gate time proportion. The coincidence interval manipulation increases the chances of overlapping of the burst with a very small gate time. The coincidence interval chosen here has been used in a similar application [4, 22] and is very small compared to the integral time scale [23].

It was found that the data rate was very sensitive to the seed generation. Too few particles and the data rate dropped because there were simply not enough particles crossing the probe volume. Too many, and the scattering all along the beam path overpowered the Doppler signal coming from the probe volume. The highest data rate was obtained with 3 jets working for 4 seconds immediately prior to running the experiment.

The LDV average velocity measurements have a peculiarity intrinsic to the sampling nature: velocity bias. When averaged, LDV readings can be biased to higher magnitudes because it takes less time for a “fast” particle to traverse the probe volume than a “slow” particle. This time difference results in more samples of at higher magnitudes. To illustrate the effect, Figure 13 was prepared. The blue line represents a simplified real time flow. It is seen that the velocity average should be the green line, however, because there are more samples at higher velocities, the average computed from the samples would be shifted towards the higher values.

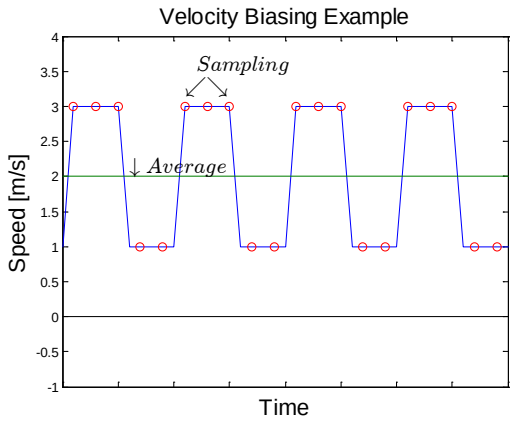

Figure 13 For the sake of simplicity, sampling seems to be regularly spaced here. Actual sampling in LDV measurements is random.

One strategy to compensate for velocity bias is to construct a weighted average that assigns a weight proportional to the gate time. That is, frequency burst that last longer are more important than short bursts. The velocity bias is corrected with this method enabling the Gatetime Weighting in the LDV controls.

$$U_i(\mathbf{x}) = \frac{\sum_n^N \tilde{u}_i(t_n;\mathbf{x})\tau_n}{\sum \tau_n} \tag{5}$$

Where:

$\tilde{u}_i(t_n;\mathbf{x})$	A sample of velocity in direction i at time t_n and positon $\mathbf{x}$
N	Total number of samples in time series
t_n	Time stamp
τ_n	Burst duration.

Figure 14 depicts the experiment control logic that was implemented with timers and relays. The experiment or run starts with a push button that set the motors in motion. The fans in the vessel spin for 22 seconds; however the data acquisition is delayed to allow the motors to reach the set speed. For experiments at 8,000 rpm, the turbulence development delay was 2 seconds. For experiments at 12,000 rpm, the delay was set to 10 seconds. The data acquisition stops when the motors shut down.

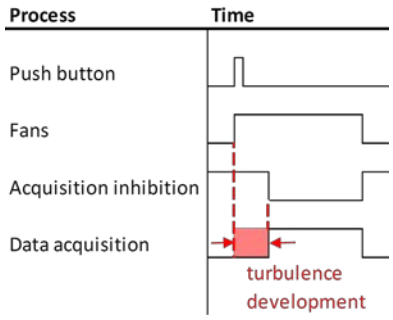

Figure 14 Experiment control logic

3.5. Experiment description

Two fan speeds were tested with 2D LDV in this work, namely 8,000 and 12,000 rpm. The motor speed was redundantly verified to be within ±200 rpm from the target speed with a photo tachometer and a stroboscopic lamp. Both speed levels used the same impeller with 20 AOA, as designed by Ravi [2]. The region under study was defined as the cubic volume located at the center of the vessel, with a length size of 60 mm, here after referred to as the test region. The center of the test region, the geometric center of the vessel, and the coordinate system origin are coincident, see Figure 15.

Four (4) run repetitions were performed at each location for the 8000 rpm. In total, more than 1400 runs where performed to scan the test region at this fan speed. The test region was discretized in even spaced lattice grid of 1cm. There were in total 343 measurement locations.

In the case of 12,000-rpm experiments, fewer locations where chosen within the region of study. As a matter of fact, the measurements were limited to one plane and the grid was evenly spaced at 1.5 cm, making a total of 25 locations. There were also fewer repetitions per location. A minimum of two (2) and a maximum of three (3) repetitions were performed at each location.

Results will be presented following this coordinate system convention. The triad depicted in Figure 15 indicates the positive direction of the X,Y, and Z axes. Notice that the Z axis and the cylindrical axis are collinear and the electrode rods are along the Y axis. The X axis will be referred to as the “horizontal” direction; the Y axis as the “vertical” direction; and the Z axis as the “cylindrical axis” in the rest of the text.

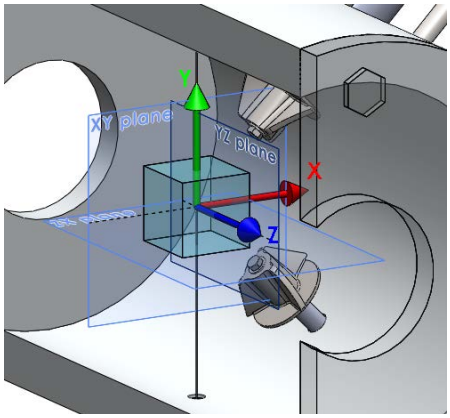

Figure 15 Test region inside the flame bomb. Notice that the cylindrical axis and the Z axis are collinear.

4. RESULTS

4.1. Organization

The results are presented in detail for a fan speed of 8000 rpm at a cross section parallel to the XY plane that cuts the vessel in two mirrored cylinders. This cross section contains the origin of the coordinate system and is perpendicular to the Z axis. The relevant overall results are discussed in this section as well, along with those pertaining to a fan speed of 12,000. However, the plots of the rest of the test region and for higher speed are left for the annexes. It was decided that the plots chosen here represent well the features observed in the study.

4.2. Average velocity

Figure 16 is an arrow or vector plot. This figure was prepared by first obtaining the average of the velocity time series for every run. Then, the measurements taken at the same location were averaged to produce one result per location. The arrow horizontal and vertical components are proportional to the local average of horizontal and vertical velocity, respectively. There is one arrow per each grid location, in other words, the test region was scanned at evenly spaced intervals of 1 cm for this fan speed. The duration of each time series is approximately 20 seconds.

An anticlockwise vortex pattern is suggested by Figure 16. The minimum average velocity is found at the center of the cross section, which is in the vicinity of the cylindrical axis according to the coordinate system used for this work. The magnitude of

the 2D average velocity increases away from the [0, 0] coordinate or in the radial direction. The vortex is visible when the average velocity data are used to create a streamline plot, Figure 17. This pattern agrees with a previous study [2].

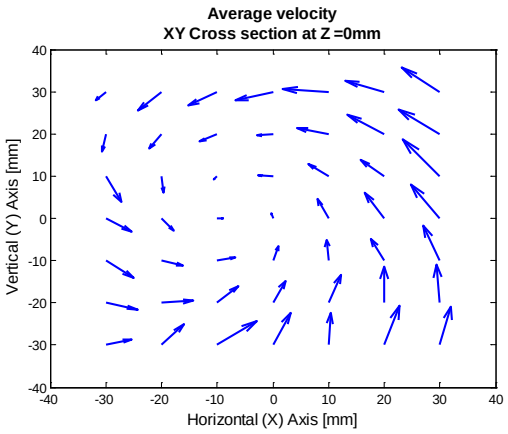

Figure 16 Average velocity vector plot at the midplane. The magnitude increases away from the (0, 0) coordinates.

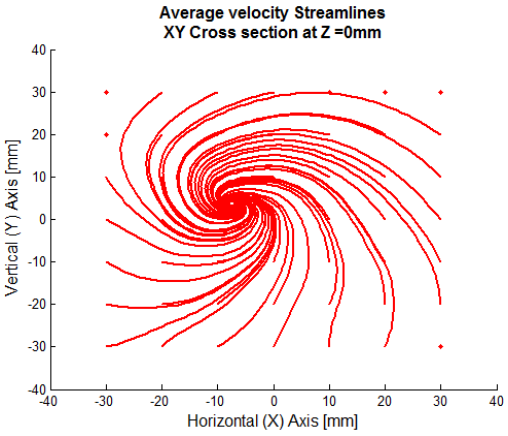

Figure 17 A vortex is well defined and evident.

The magnitude of the average velocities and their distribution is better described in a contour plot like Figure 18 and Figure 19. Roughly speaking, the plots are divided diagonally in two zones that have particles moving in opposite directions at each side of the line labeled 0. The particles converge to the diagonal division.

The highest average velocity component in the horizontal direction is found in the upper right corner of Figure 18. The particles there are moving something between 0.6 and 0.8 m/s in direction to the left. The fastest particles moving in the opposite direction are in the bottom left corner, clocking 0.4-0.6 m/s.

A similar inspection of the vertical velocity component shows that the highest average vertical velocity zone is the bottom right corner of Figure 19, ranging 0.8-1.0 m/s. These particles are moving upwards, while particles on the other side of the diagonal move downwards with a maximum speed of 0.6-0.4 m/s.

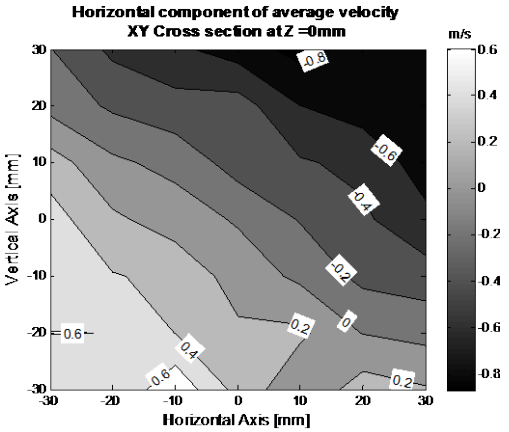

Figure 18 Average horizontal velocity contour plot. Labels in m/s. Negative sign denotes particle moving to the left.

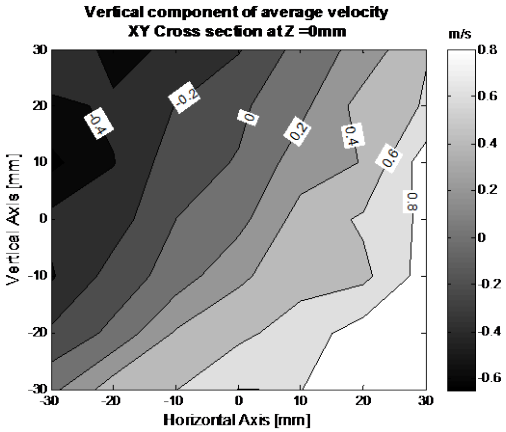

Figure 19 Average vertical velocity contour plot. Labels in m/s. Negative sign indicates particle moving downwards.

Both horizontal and vertical components can be combined in a 2D vector. Figure 20 presents the magnitude of the resultant 2D average velocity vector. The contours shown here complement the qualitative description of the flow field in Figure 16. The ideal scenario for turbulent spherical flame speed experiments involves zero mean flow. It is clear that the average velocity results presented up to this point do not comply with this criterion, at least on the local scale. However, the mean average velocity in the horizontal and vertical components is negligible not only in the cross section discussed in the previous figures, but also in the entire test region.

Since the 2D average velocity seems to be function of radial distance away from the vortex eye, a crude estimation of the rigid body rotation speed can be obtained by choosing a radius and a tangential velocity. A radius of 3 cm and a tangential velocity of 1.1 m/s was assumed to calculate a rotational speed of 36.66 rad/s, or 350 rpm.

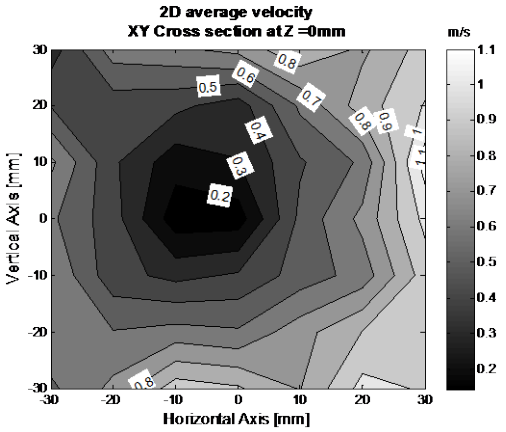

Figure 20 2D average velocity magnitude at the midplane. The eye of the vortex has the lowest magnitude while the outer edges are the fastest. This profile resembles rigid body rotation.

4.3. Axial velocity

It is possible to get insight on the velocity component that was not measured by invoking the incompressible flow assumption, the commute properties of the divergence and time averaging operators, eq. (6). It is also necessary to assume the flow is statistically stationary. The velocity magnitudes found so far are negligible compared to the sound speed at room temperature, so the incompressibility claim should be safe. The turbulence was allowed to develop before acquiring readings, and the run time is very large compared to integral time scale, therefore the stationary flow assumption is not unreasonable. This exercise should at least reveal some of the tridimensional features of

the flow, even if it is assembled from independent local measurements that are not simultaneous. The result is displayed in Figure 21. Most of the test region was found to have a mean velocity component in the positive Z direction. The color bar shows the magnitude of the curl. The overall test region average velocity in the Z direction is 0.40 m/s.

$$\overline{\nabla \bullet \tilde{\mathbf{u}}(t;\mathbf{x})} = \nabla \bullet (\overline{\mathbf{U}(\mathbf{x})} + \cancel{\overline{\mathbf{u}(t,\mathbf{x})}}) = \nabla \bullet \mathbf{U}(\mathbf{x}) = 0 \tag{6}$$

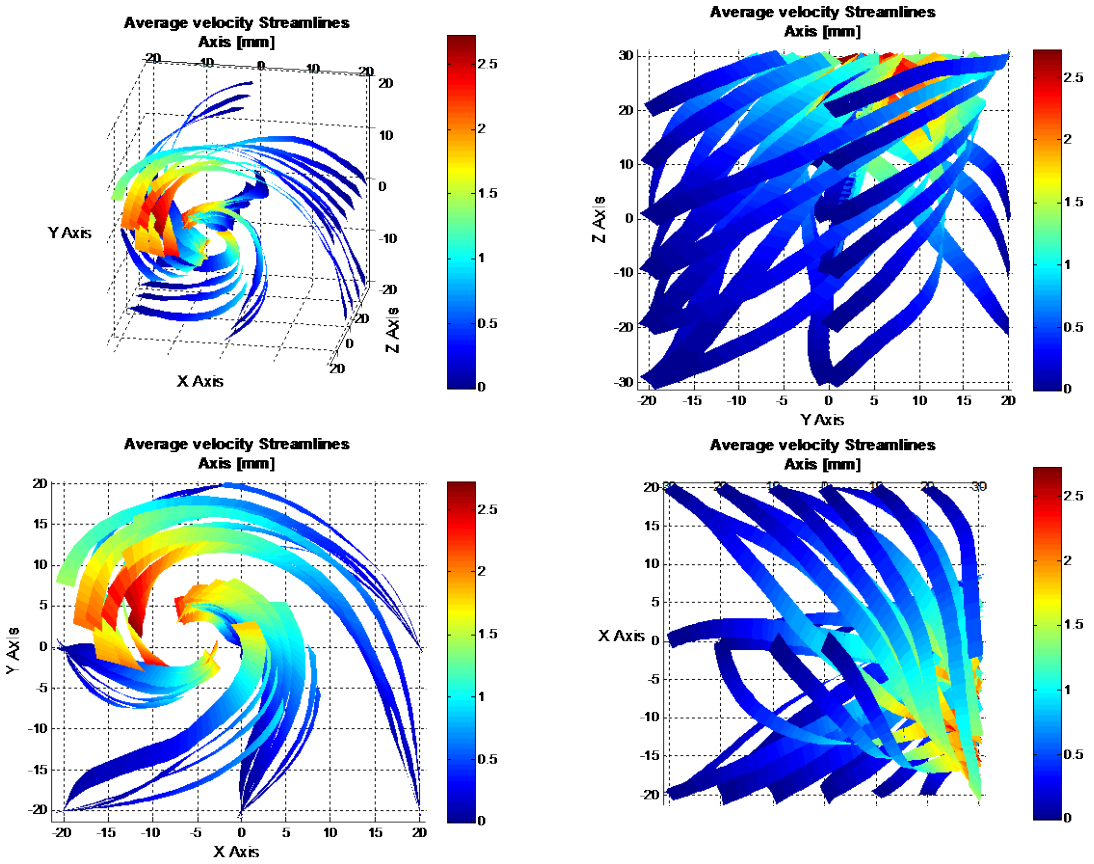

Figure 21 Stream-ribbon plot. The axis component was calculated assuming incompressible flow and central difference estimates for the divergence. Warm colors indicate higher curl value. The tridimensional character of the vortex is revealed by the streamlines.

4.4. Higher moments

The skewness and the kurtosis were computed for every run. The overall average kurtosis was 3.41 and 3.37 for the horizontal and vertical direction, respectively, and it was found very uniform in the entire test region. The kurtosis of a Gaussian distribution is 3.0, and therefore we can say the “peakness” of “flatness” of the velocity measurements resembles a Gaussian distribution.

The skewness was on average negligible for the overall test region, but a distinctive distribution was observed when the results were assembled in contour plots, Figure 22 and Figure 23. A zero skewness distribution has symmetric tails. A negative skewness means a heavier left tail, while the opposite is true for positive skewness. The plots are divided in two halves. One half has positive skewness while the other half has negative skewness. A relatively narrow band of near zero skewness separates these two zones. The nature of this skewness distribution is not evident to the author.

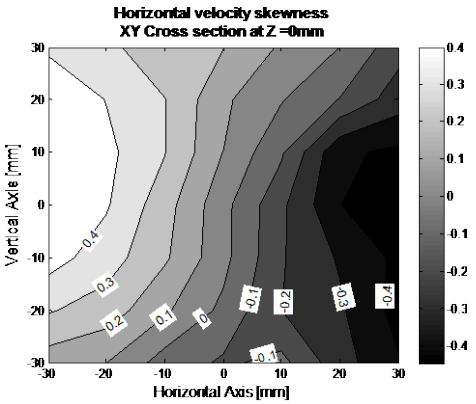

Figure 22 Horizontal velocity skewness. Heavier right tails in the velocity distribution were concentrated at negative horizontal coordinates.

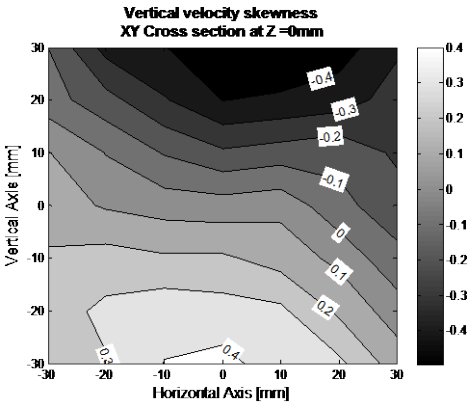

Figure 23 Vertical velocity skewness. A very ordered pattern was found in the spatial distribution of the vertical velocity skewness.

4.5. Turbulence fluctuation

The turbulence fluctuation rms in the horizontal and vertical directions is presented in Figure 24 and Figure 25, respectively, per eq. (7). In both cases, the turbulence fluctuation is less intense at the center of the cross section, near the coordinates [0, 0]. The fluctuation magnitude goes from 1.5 m/s to 1.9 m/s approximately in this plot. The test region overall average rms fluctuation is 1.60 and 1.63 m/s in the horizontal and vertical directions, respectively. These results are 8% higher than what was found in an earlier study [2] but agrees very well with the simulation of an independent group [16].

$$u_{i,rms}(\mathbf{x}) = \overline{u_i^2}^{1/2}(\mathbf{x}) = \sqrt{\frac{1}{N}\sum_{n=1}^{N}(u_i(t_n;\mathbf{x}))^2} \tag{7}$$

Where:

$u_{i,rms}(\mathbf{x})$ Turbulence fluctuation rms in direction i at positon $\mathbf{x}$

N	Total number of samples in time series
t_n	Time stamp

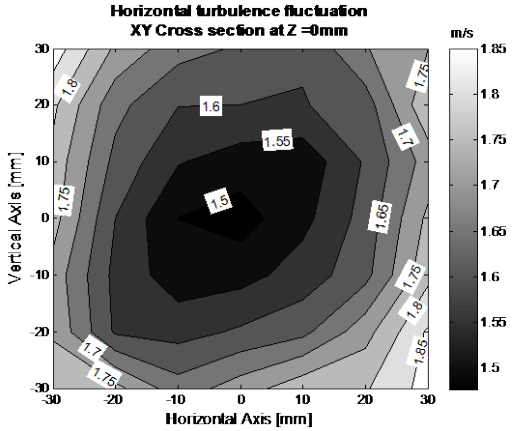

Figure 24 Horizontal turbulence fluctuation at midplane. The rms value increases radially away from the vortex eye.

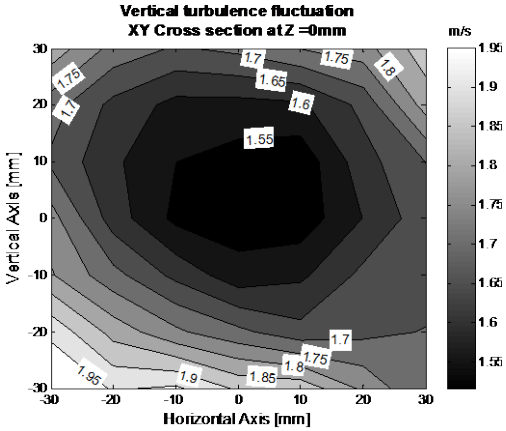

Figure 25 Vertical turbulence fluctuation at midplane. The rms value increases radially away from the vortex eye.

The turbulence fluctuation homogeneity is defined as the ratio of the local turbulence fluctuation rms to the overall spatial average, eqs. (8) and (9). The ideal case would be to have a unity homogeneity everywhere, which implies that the local turbulence fluctuation and the overall average are numerically identical in the entire test region. However a deviation of ±10% from the overall average is acceptable. The flow is in general homogenous, with the exemption of the outer margin, where the turbulence fluctuation exceeds the test region average by more than 10%; see Figure 26 and Figure 27. The turbulence fluctuation in the vertical direction is slightly less homogenous. Furthermore, the rms of the residual local turbulence fluctuation and the spatial average is 0.11 and 0.13 in the horizontal and vertical directions, respectively.

$$H_i(\mathbf{x}) = \frac{u_{i,rms}(\mathbf{x})}{\overline{u_{i,rms}}} \tag{8}$$

$$\overline{u_{i,rms}} = \frac{1}{M}\sum_{1}^{M} u_{i,rms}(\mathbf{x}_m) \tag{9}$$

Where:

$H_i(\mathbf{x})$	Turbulence homogeneity in direction i at location $\mathbf{x}$
$\overline{u_{i,rms}}$	Spatial average of the turbulence fluctuation in direction i
$\mathbf{x}_m$	Coordinates of the mth sampling location
M	Total of sampling points in test region grid

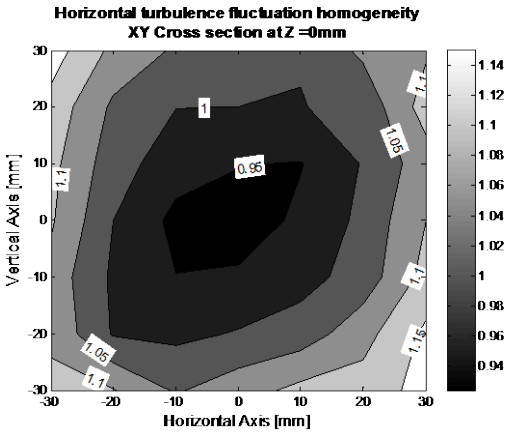

Figure 26 Horizontal turbulence fluctuation homogeneity

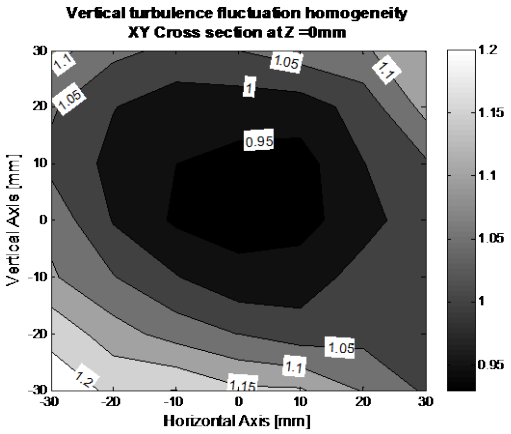

Figure 27 Vertical turbulence fluctuation homogeneity

Turbulent spherical flame experiments demand no preferential direction in the turbulence fluctuation. The isotropy tests the relative strength of the turbulence fluctuation components at each location. In this study, only the horizontal and vertical

components were considered since no simultaneous measurements exist for the third component, eq. (10). It was found that the turbulence fluctuation had no preferential direction in general, see Figure 28. The isotropy was also observable in the $\tilde{u}_x$ Vs. $\tilde{u}_y$ scatter plots, of which Figure 29 is an example. Notice the relatively round shape of the scatter plot, where the fluctuation in both directions is comparable. Furthermore, this scatter plot also indicates that $\tilde{u}_x$ is not correlated with $\tilde{u}_y$, i.e. they are independent. This claim is confirmed later on with the Reynolds stress results.

$$I_{xy}(\mathbf{x}) = \frac{u_{x,rms}(\mathbf{x})}{u_{y,rms}(\mathbf{x})} \tag{10}$$

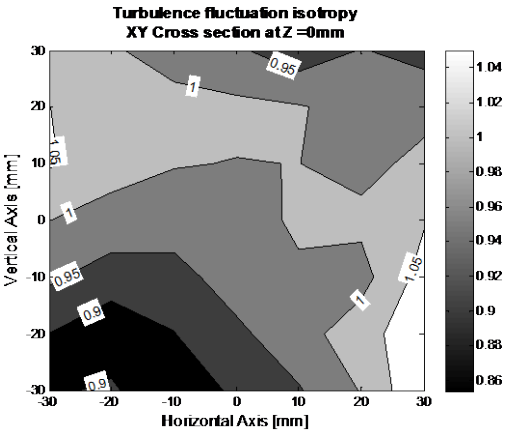

Figure 28 Turbulence fluctuation isotropy. The rms values of the turbulence fluctuation rms in the horizontal and vertical direction are almost identical at every location.

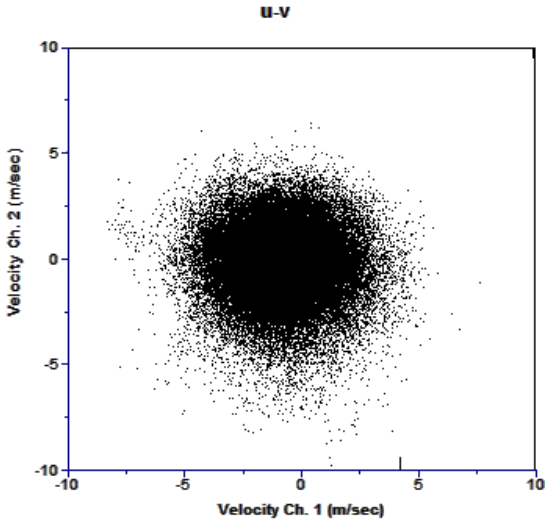

Figure 29 $\tilde{u}_x$ Vs. $\tilde{u}_y$ scatter plot of run#1100. The instantaneous values of the velocity components are ploted against each other. This plot is possible thanks to the coincident (simultanesous) measurement of the both components.

4.6. Ratio of average velocity over turbulence fluctuation rms

So far, the average velocity and the turbulence fluctuation have been discussed independently. The average velocity magnitude should be ideally zero but at most 10% of the rms of turbulence fluctuation. Figure 30 and Figure 31 have been prepared to show the spatial distribution of the ratio of the average velocity over the turbulence fluctuation rms in the horizontal and vertical directions, respectively. It can be noticed that the average velocity magnitude meets the target in a narrow band. Most of the visible area is characterized with average velocity level that is between 20 and 50% of the turbulence fluctuation rms. The figures shown here are representative of what was observed in the rest of the test region.

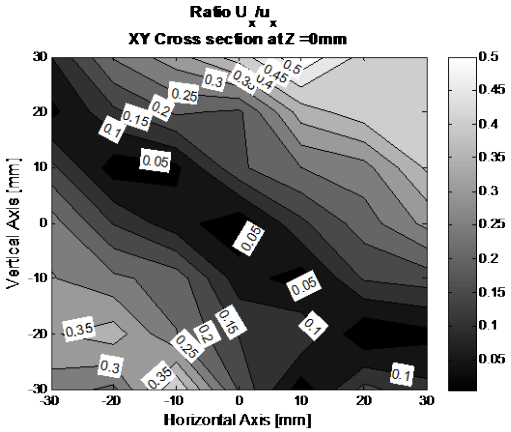

Figure 30 Ratio of average velocity to turbulence fluctuation in the horizontal direction. Most of the area presents not acceptable ratios.

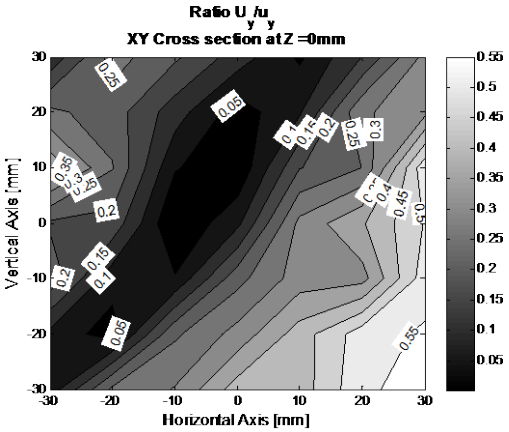

Figure 31 Ratio of average velocity to turbulence fluctuation in the vertical direction. Again the only a narrow band that runs diagonally has low enough ratios.

4.7. Reynolds stresses

Reynolds stresses calculation was enabled by the simultaneous measurements of the vertical and horizontal components of velocity at every location. Both of the normal stresses $\overline{u_x u_x}$ and $\overline{u_y u_y}$ are significantly larger than the shear stress $\overline{u_x u_y}$. The contour maps exhibits a radial profile in Figure 32, Figure 33 and Figure 34. As of matter of fact, this finding is positive, since for homogenous isotropic turbulence the shear Reynolds stress $\overline{u_x u_y}$ vanishes [24, 25].

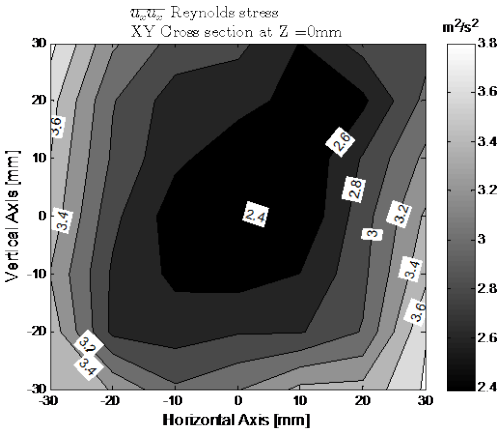

Figure 32 Normal stress $\overline{u_x u_x}$. The radial distribution reminds that of the turbulence fluctuation rms.

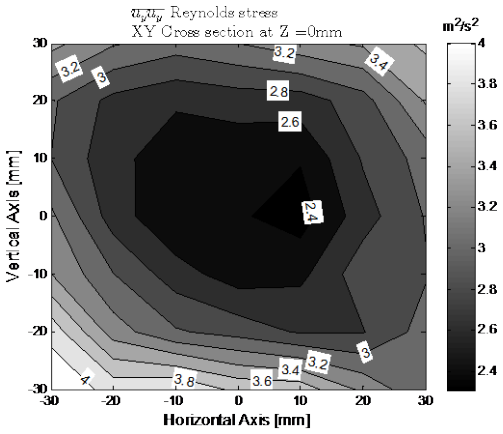

Figure 33 Normal stress $\overline{u_y u_y}$. Notice that the magnitude of the normal stresses $\overline{u_x u_x}$ and $\overline{u_y u_y}$ both have considerably larger magnitudes than the shear stress.

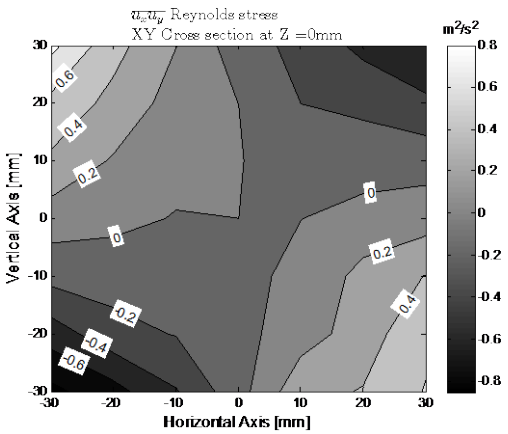

Figure 34 Reynolds shear stress. Turbulence theory predicts that the shear stress is zero for homogenous isotropic turbulence [24, 25].

4.8. Time scales

Before the time scales are discussed, the long term transient or oscillation in the turbulence fluctuation should be introduced. Figure 35 presents a time series of turbulence fluctuations. The real time data are shown in blue, while the red line has the same information after being aggressively filtered. The mean of the values of this series, in green, is zero, however there is a noticeable, low-frequency oscillation. For the first five seconds, the red line stays mostly above zero and for the last 9 seconds, the red line hardly leaves the negative side.

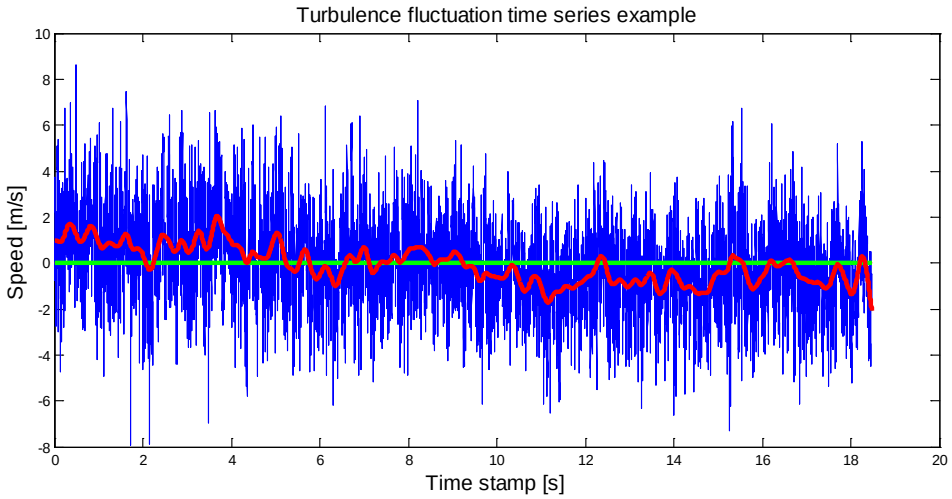

Figure 35 Turbulence fluctuation in horizontal direction. Run # 1656 at coordinates (0,10,30)mm. The green line is the average. The data in blue has been filtered and plotted in red. Notice the sluggish oscillation of the filtered signal above and below the average.

The low-frequency wobble described above is extremely slow compared to flame speed experiments, which are in the realm of milliseconds in duration. Although, strictly speaking, this oscillation is part of the temporal coherence of the turbulence, the full length of the time series wasn't used for the calculation of the temporal correlation coefficient and thus the integral time scale. Instead, shorter segments were employed, just enough to get the correlation coefficient to vanish.

The time scale was investigated in several locations by getting the coefficient of temporal correlation of which Figure 36 is an example. The integral time scale Λ_t is numerically equal to the area under the curve of the temporal correlation coefficient, eq. (11). The Taylor microscale λ_t is defined as the curvature of the autocorrelation peak at

$\tau = 0$, eq.(12) [17]. The integral time scale is on the order of 10 ms, while the Taylor microscale range from 0.4-2.0 ms.

$$\Lambda_t \equiv \int_0^\infty r(\tau)\, d\tau \tag{11}$$

$$\lambda_t^2 \equiv -2 \Big/ \left. \frac{\partial^2 r}{\partial \tau^2} \right|_{\tau=0} \tag{12}$$

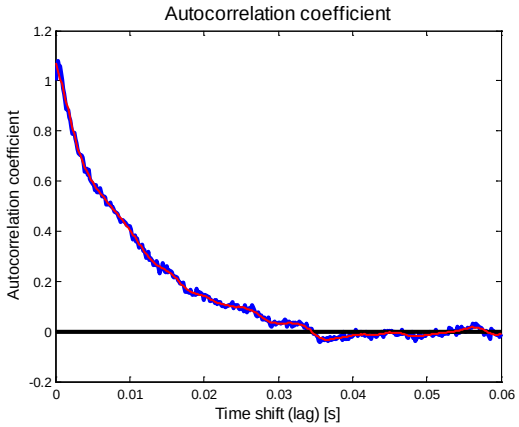

Figure 36 Autocorrelation of run # 1592 vertical turbulent fluctuation component. Notice that after 30 ms, the turbulence becomes uncorrelated with itself, i.e. the correlation coefficient goes to zero.

The time scales at different locations are condensed in Table 4. The eddy turn over integral time scale reported Ravi et al [2] is at least three times greater than the integral time scales found here. It must be reminded that in their study, the macro scale was defined as the ratio of the turbulent kinetic energy and its dissipation rate, so the difference does not imply a conflict.

Table 4 Time scales at different locations. Fans running at 8000 rpm

Run #	Location	Integral time scale [ms]		Taylor microscale [ms]	
		Horizontal	Vertical	Horizontal	Vertical
285	0, 0, 0	13.5	12.5	0.60	0.45
1112	30, 0, 0	10.2	8.5	0.53	0.38
943	-30, 0, 0	10.5	8.8	1.66	0.46
1015	0, 30, 0	11.3	11.6	1.36	2.09
1040	0, -30, 0	13.2	15.9	1.9	1.95
436	0, 0, 30	12.4	11.4	1.85	1.95
1592	0, 0, -30	10.1	9.9	1.43	1.43

4.9. Results at 12,000 rpm

The experimental settings for the tests at 12,000 rpm remained unchanged with the exemption of the delay time in the acquisition after the fan start. It took the motors considerably more time to approach the set speed from stop. The acquisition started 10 seconds after the motors were energized. Only one plane was studied, Z=0 mm, and not the entire test region. The grid spacing was widened to 1.5 cm.

The reader is invited to look in Appendix B for the plots of the measurements at 12,000 rpm. The arithmetic mean of all the locations scanned is assembled in Table 5, where both fan speed levels are included for easy comparison. The average velocity increased in both directions when the fan speed was cranked up, but stayed modest. The turbulence fluctuation rms increased linearly with fan speed. A 50% increase in fan speed translated to the same proportion in the turbulence fluctuation rms, in agreement with previous studies [4, 7]. The axial average velocity that was calculated, not measured, increased more than three fold. The relative magnitude of the average velocity did not change with

respect to the turbulent fluctuation rms. The skewness, flatness, turbulence isotropy, and shear Reynolds stress remain invariant. The Reynolds shear stress scaled as $(1.5)^2$, following the behavior of the turbulence rms.

Table 5 Results summary. Arithmetic mean of all locations

Parameter		Formula	8,000 rpm		12,000	
			$i = x$	$i = y$	$i = x$	$i = y$
Average velocity	m/s	$U_i(\mathbf{x})$	-0.07	0.21	-0.17	0.41
Turbulence fluctuation	m/s	$u_{i,rms}(\mathbf{x})$	1.60	1.63	2.43	2.53
Axial average velocity	m/s	$U_z(\mathbf{x})$	0.40		1.35	
Ratio average/fluctuation		$\|U_i(\mathbf{x})\| / u_{i,rms}(\mathbf{x})$	0.22	0.24	0.24	0.24
Skewness		$\frac{1}{N}\sum_{n=1}^{N}(u_i(t_n;\mathbf{x}))^3 \Big/ \left(u_{i,rms}\right)^3$	0.03	0.01	-0.03	0.04
Flatness		$\frac{1}{N}\sum_{n=1}^{N}(u_i(t_n;\mathbf{x}))^4 \Big/ \left(u_{i,rms}\right)^4$	3.41	3.37	3.45	3.39
Turbulence isotropy		$u_{x,rms}(\mathbf{x}) / u_{y,rms}(\mathbf{x})$	0.98		0.96	
Turbulence homogeneity		$u_{i,rms}(\mathbf{x}) / \overline{u_{i,rms}}$	1.00	1.00	1.00	1.00
Normal Reynold stress	m^2/s^2	$\overline{u_i(\mathbf{x})u_i(\mathbf{x})}$	2.79	2.81	6.77	6.86
Shear Reynolds stress	m^2/s^2	$\overline{u_x(\mathbf{x})u_y(\mathbf{x})}$	0.01		0.01	
Rigid body vortex speed	rpm		350		490	

The simple arithmetic mean can be misleading for parameters that have positive and negative values, because the averaging hides the deviations from zero. A modified table was prepared with the absolute values of selected parameters, see Table 6. The average velocity now shows a different story, because it deviates from zero more than previous figure. The skewness and the shear stress also increase significantly.

Table 6 Results summary. Arithmetic mean of absolute values all locations

Parameter		Formula	8,000 rpm		12,000	
			$i = x$	$i = y$	$i = x$	$i = y$
Average velocity	m/s	$U_i(\mathbf{x})$	0.35	0.40	0.58	0.61
Axial average velocity	m/s	$U_z(\mathbf{x})$	0.41		1.35	
Skewness		$\frac{1}{N}\sum_{n=1}^{N}(u_i(t_n;\mathbf{x}))^3 \Big/ \left(u_{i,rms}\right)^3$	0.23	0.20	0.26	0.23
Shear Reynolds stress	m^2/s^2	$\overline{u_x(\mathbf{x})u_y(\mathbf{x})}$	0.20		0.68	

5. CONCLUSIONS

The results obtained here agree with the work of Ravi [2] to the extent the two studies overlap in scope, despite the fact that different techniques were employed. The present work went further by extending the measurement to a tridimensional space and by testing an additional level of fan speed.

The results of the three-dimensional test region were organized in two dimensional plots or cross sections. The cross sections exhibited features that were fairly consistent throughout the entire test region. Radial patterns in the spatial distribution of the turbulence statistics were commonly encountered with an axis of symmetry along the cylindrical axis of the vessel.

The turbulence fluctuation rms was found to be fairly homogenous and isotropic throughout the test region, although the magnitude recorded with the LDV was slightly higher than the PIV. The isotropy of the turbulence fluctuation was ratified by the $\overline{u_x u_y}$ Reynolds stress and the scatter plots of $\tilde{u}_x$ Vs. $\tilde{u}_y$.

The average velocity magnitudes were higher than expected, in the two directions that were directly measured, i.e. horizontal and vertical. As a matter of fact, the turbulence intensity ratio is within the target range only in the vicinity of the cylindrical axis. The third component, in the axial direction, was inferred invoking mass conservation. While

the simple arithmetic spatial mean of the vertical and horizontal average velocity results practically null, the axial component has a resultant mean flow of 0.4 m/s.

A vortical structure spinning around the cylindrical axis was present was revealed by the average velocity streamlines. It was estimated that the vortex swirls at 350 rpm with the fans running at 8,000 rpm and nearly at 500 rpm with the fans spinning at 12,000 rpm.

The integral time scale was at most one third of the macro time scale reported by Ravi [2]. The values however not necessarily are expected to match since to different approaches were taken. The present study evaluated the integral time scale from autocorrelation while Ravi estimated it as the ratio of the turbulent kinetic energy and the dissipation rate.

The turbulence fluctuation rms scaled with the fan speed as expected, in agreement with the literature. However, other parameters such as average velocity and the axial velocity deteriorated.

In summary, while the flow presents some of the characteristics desired for spherical turbulent flame speed experiments, it has opportunities that can be addressed in the next iteration of flame bomb, perhaps shaping the bomb and fan arrangement closer to a regular polyhedron as other groups have tried [8, 13, 16, 26].

REFERENCES

[1] De Vries, J., 2009, "A study on spherical expanding flame speeds of methane, ethane, and methane/ethane mixtures at elevated pressures.," PhD, Texas A&M University, College Station, Texas.

[2] Ravi, S., Peltier, S. J., and Petersen, E. L., 2013, "Analysis of the impact of impeller geometry on the turbulent statistics inside a fan-stirred, cylindrical flame speed vessel using PIV," Experiments in Fluids, 54(1).

[3] Ravi, S., 2014, "Measurement of turbulent flame speeds of hydrogen and natural gas blends (C1-C5 alkanes) using a newly developed fan-stirred vessel," PhD, Texas A&M University, College Station, Texas, U.S.A.

[4] Birouk, M., Sarh, B., and Gökalp, I., 2003, "An Attempt to Realize Experimental Isotropic Turbulence at Low Reynolds Number," Flow, Turbulence and Combustion, 70(1-4), pp. 325–348.

[5] Kwon, S., 1991, "Flame surface properties of neutrally stable premixed flames in isotropic turbulence," PhD, University of Michigan, Ann Arbor.

[6] Fansler, T. D., and Groff, E. G., 1990, "Turbulence characteristics of a fan-stirred combustion vessel," Combustion and Flame, 80(3-4), pp. 350-354.

[7] Brutscher, T., Zarzalis, N., and Bockhorn, H., 2002, "An experimentally based approach for the space-averaged laminar burning velocity used for modeling premixed turbulent combustion," Proceedings of the Combustion Institute, 29(2), pp. 1825-1832.

[8] Galmiche, B., Mazellier, N., Halter, F., and Foucher, F., 2014, "Turbulence characterization of a high-pressure high-temperature fan-stirred combustion vessel using LDV, PIV and TR-PIV measurements," Experiments in Fluids, 55(1), pp. 1-20.

[9] Kido, H., Nakahara, M., Nakashima, K., and Hashimoto, J., 2002, "Influence of local flame displacement velocity on turbulent burning velocity," Proceedings of the Combustion Institute, 29(2), pp. 1855-1861.

[10] Shy, S. S., I, W. K., and Lin, M. L., 2000, "A new cruciform burner and its turbulence measurements for premixed turbulent combustion study," Experimental Thermal and Fluid Science, 20(3-4), pp. 105-114.

[11] Leisenheimer, B., and Leuckel, W., 1996, "Self-Generated Acceleration of Confined Deflagrative Flame Fronts∗," Combustion Science and Technology, 118(1-3), pp. 147-164.

[12] Weiß, M., Zarzalis, N., and Suntz, R., 2008, "Experimental study of Markstein number effects on laminar flamelet velocity in turbulent premixed flames," Combustion and Flame, 154(4), pp. 671–691.

[13] Ali, Y. B., 1995, "Fundamentals of Turbulent Combustion Related to Gasoline Engines," PhD, University of Leeds.

[14] Abdel-Gayed, R. G., Al-Khishali, K. J., and Bradley, D., 1984, "Turbulent burning velocities and flame straining in explosions," Proceedings of the Royal Society of London. Series A, Mathematical and physical sciences, 391(1801), pp. 393-414.

[15] Chaudhuri, S., Wu, F., Zhu, D., and Law, C. K., 2012, "Flame Speed and Self-Similar Propagation of Expanding Turbulent Premixed Flames," Physical Review Letters, 108(4), p. 044503.

[16] Davani, A. A., and Ronney, P. D., "A Jet-Stirred Apparatus for Turbulent Combustion Experiments," Proc. 9th U. S. National Combustion Meeting.

[17] Kundu, P. K., Cohen, I. M., and Dowling, D. R., 2012, "Chapter 12 - Turbulence," Fluid Mechanics (Fifth Edition), Academic Press, Boston, pp. 541-620.

[18] Ramond, A., and Millan, D., 2000, "Measurements and treatment of LDA signals, comparison with hot-wire signals," Experiments in Fluids, 28(1), pp. 58-63.

[19] Bell, W., "Spectral analysis of laser velocimeter data with the slotted correlation method," Proc. Proceedings of the AIAA/ASME Fourth Fluid Mechanics, Plasma Dynamics and Lasers Conference.

[20] TSI, 2012, "Phase Doppler Particle Analyzer (PDPA) / Laser Doppler Velocimeter (LDV) Operations Manual," No. P/N 1990048.

[21] TSI, 2010, "Model 9306 Six- Jet Atomizer Owner's Manual," No. P/N 1990143.

[22] Bédat, B., and Cheng, R. K., 1995, "Experimental study of premixed flames in intense isotropic turbulence," Combustion and Flame, 100(3), pp. 485-494.

[23] Belmabrouk, H., 1998, "Taylor length scale measurement by laser Doppler velocimetry," Experiments in Fluids, 25(1), pp. 69-76.

[24] Bradley, D., Gaskell, P. H., and Gu, X. J., 1994, "Application of a reynolds stress, stretched flamelet, mathematical model to computations of turbulent burning velocities and comparison with experiments," Combustion and Flame, 96(3), pp. 221-248.

[25] Libby, P. A., 1996, Introduction to turbulence, Washington, D.C. : Taylor & Francis, c1996.

[26] Mével, R., Lafosse, F., Chaumeix, N., Dupré, G., and Paillard, C. E., 2009, "Spherical expanding flames in H2–N2O–Ar mixtures: flame speed measurements and kinetic modeling," International Journal of Hydrogen Energy, 34(21), pp. 9007-9018.

APPENDIX A

PLOTS OF MEASUREMENTS AT 8,000 RPM

Horizontal component of average velocity at 8,000 rpm

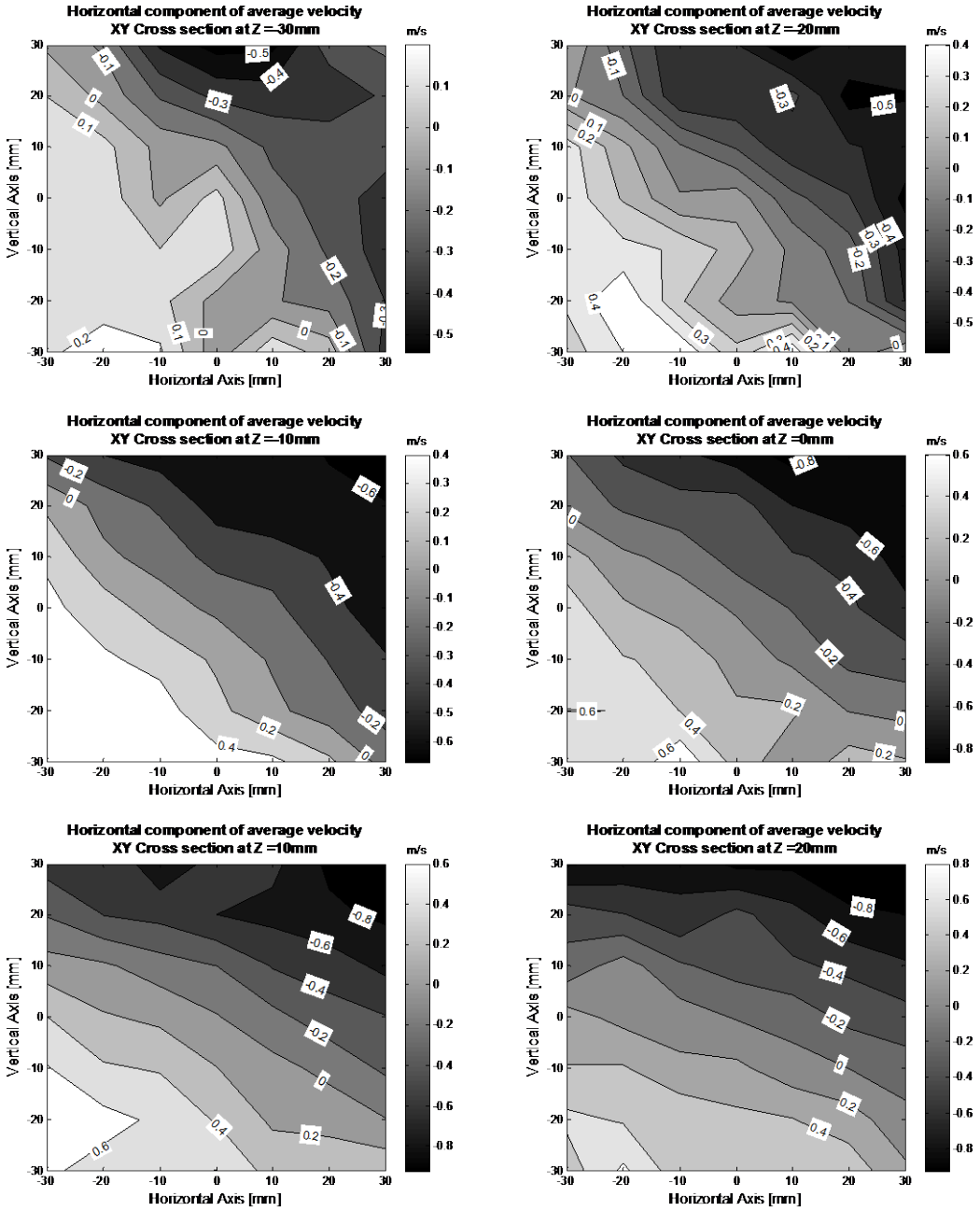

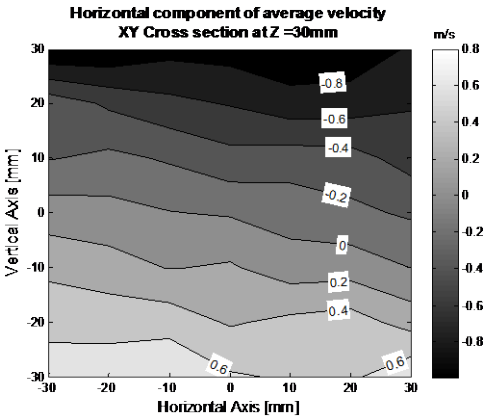

Vertical component of average velocity at 8,000 rpm

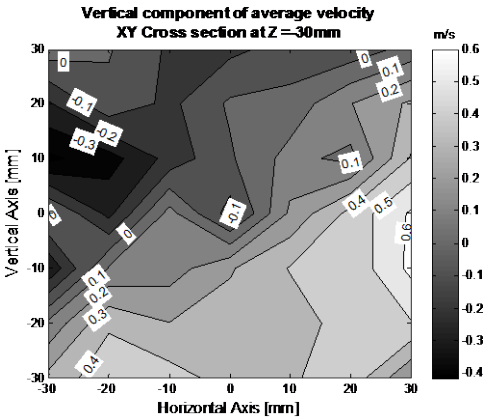

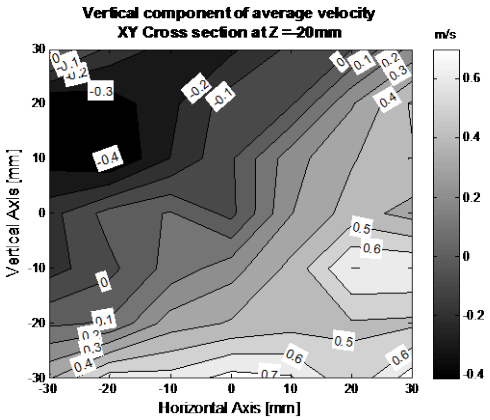

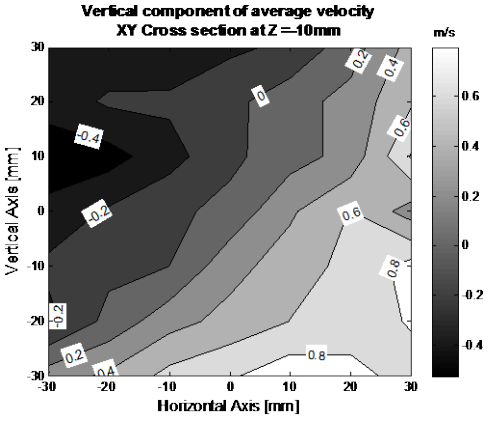

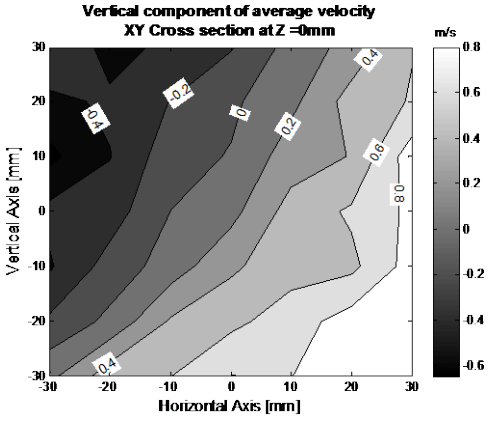

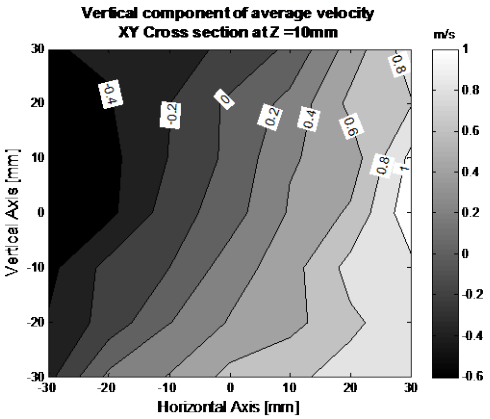

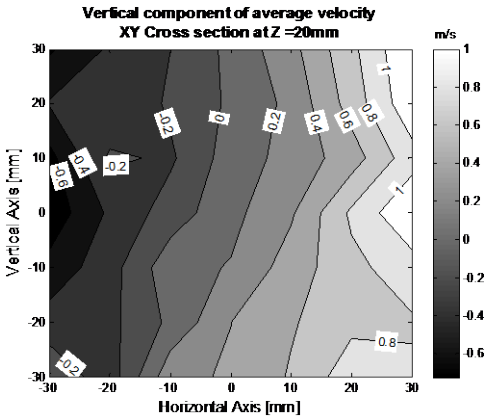

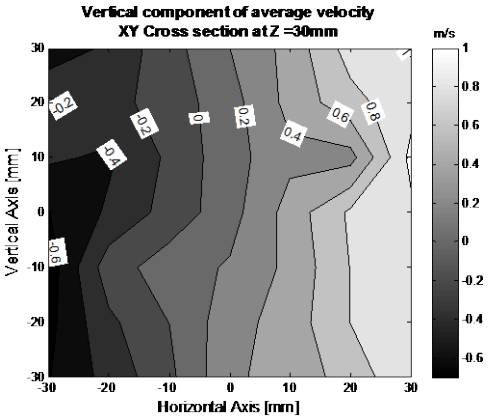

Horizontal component of turbulence fluctuation at 8,000 rpm

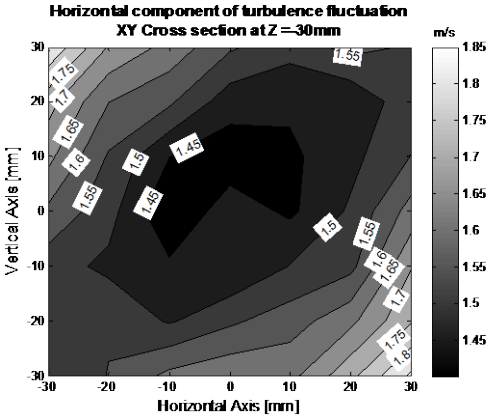

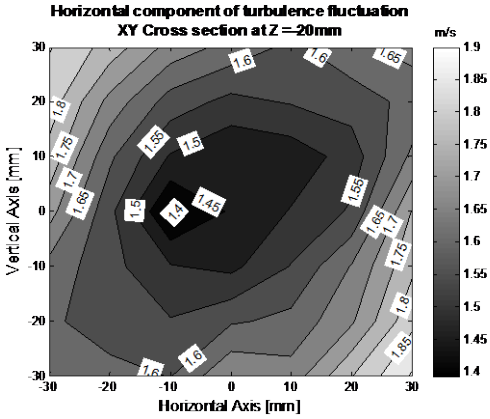

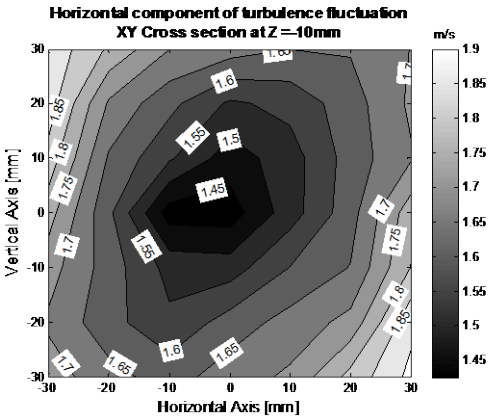
Horizontal component of turbulence fluctuation
XY Cross section at Z =-10mm
m/s
Vertical Axis [mm]
Horizontal Axis [mm]

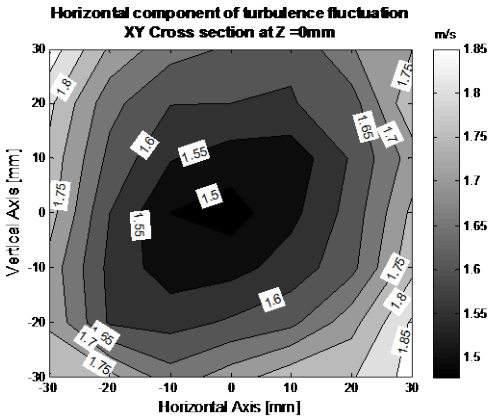
Horizontal component of turbulence fluctuation
XY Cross section at Z =0mm
m/s
Vertical Axis [mm]
Horizontal Axis [mm]

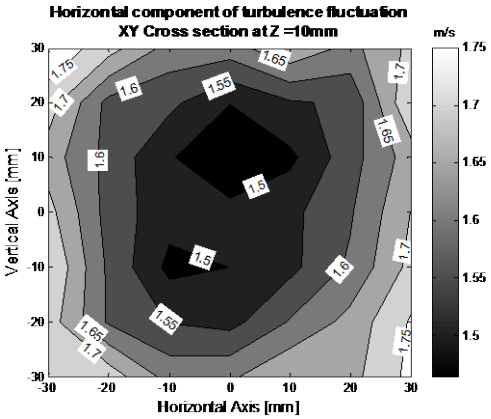
Horizontal component of turbulence fluctuation
XY Cross section at Z =10mm
m/s
Vertical Axis [mm]
Horizontal Axis [mm]

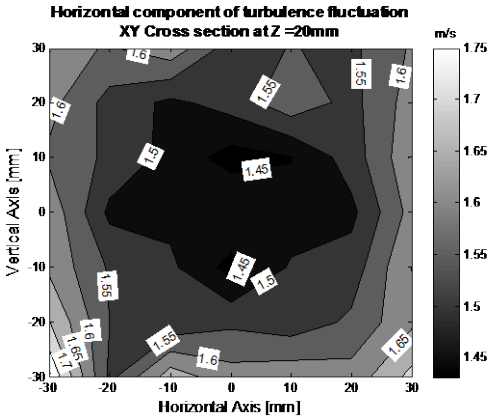
Horizontal component of turbulence fluctuation
XY Cross section at Z =20mm
m/s
Vertical Axis [mm]
Horizontal Axis [mm]

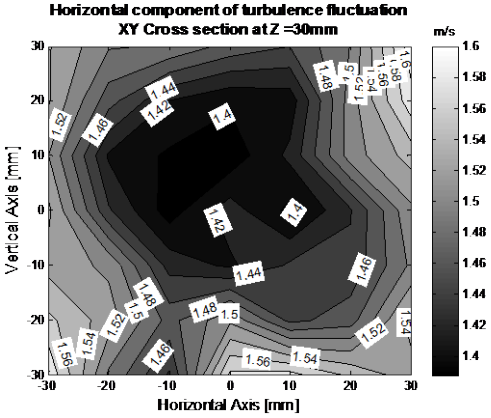
Horizontal component of turbulence fluctuation
XY Cross section at Z =30mm
m/s
Vertical Axis [mm]
Horizontal Axis [mm]

Vertical component of turbulence fluctuation at 8,000 rpm

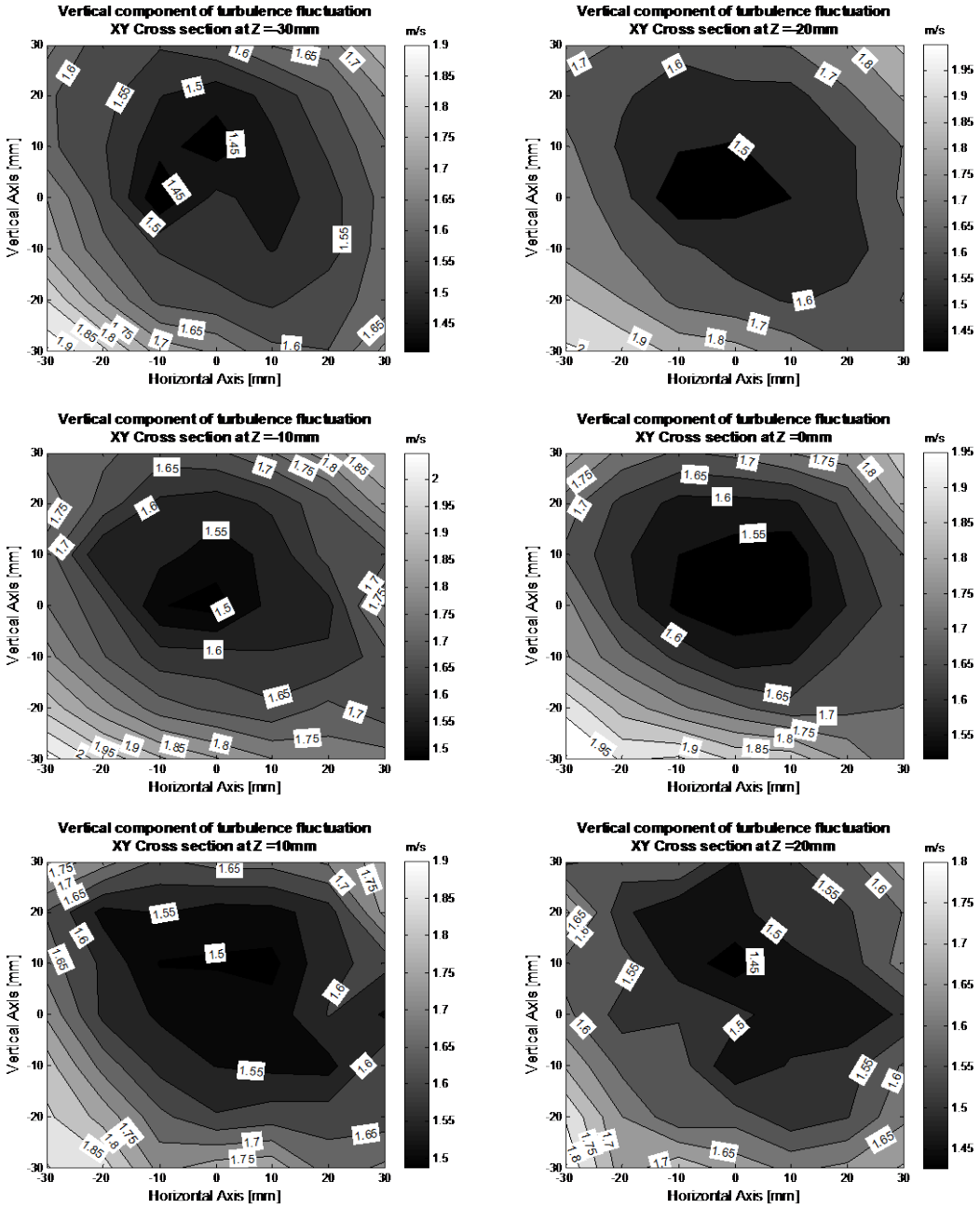

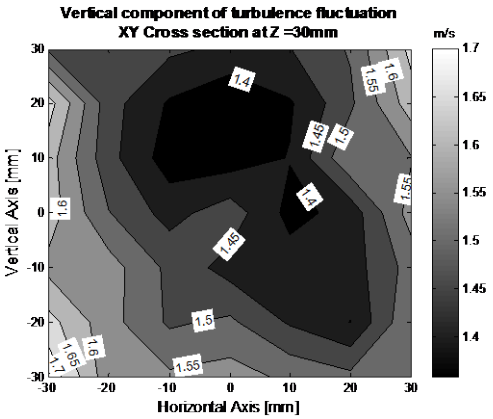

Ratio of average over fluctuation in horizontal direction at 8,000 rpm

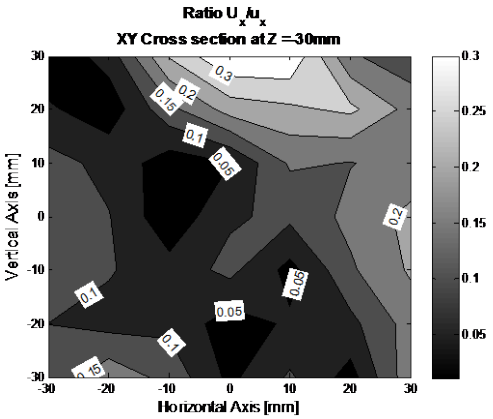

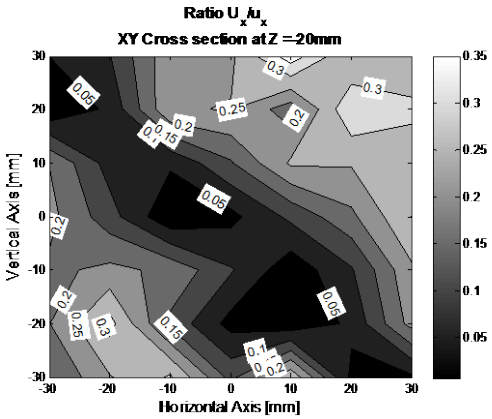

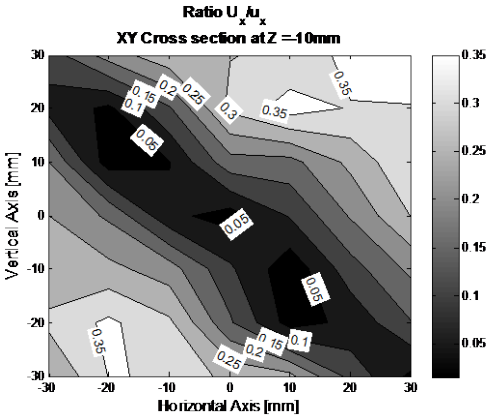

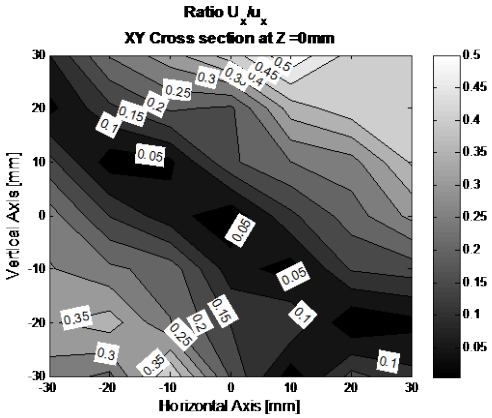

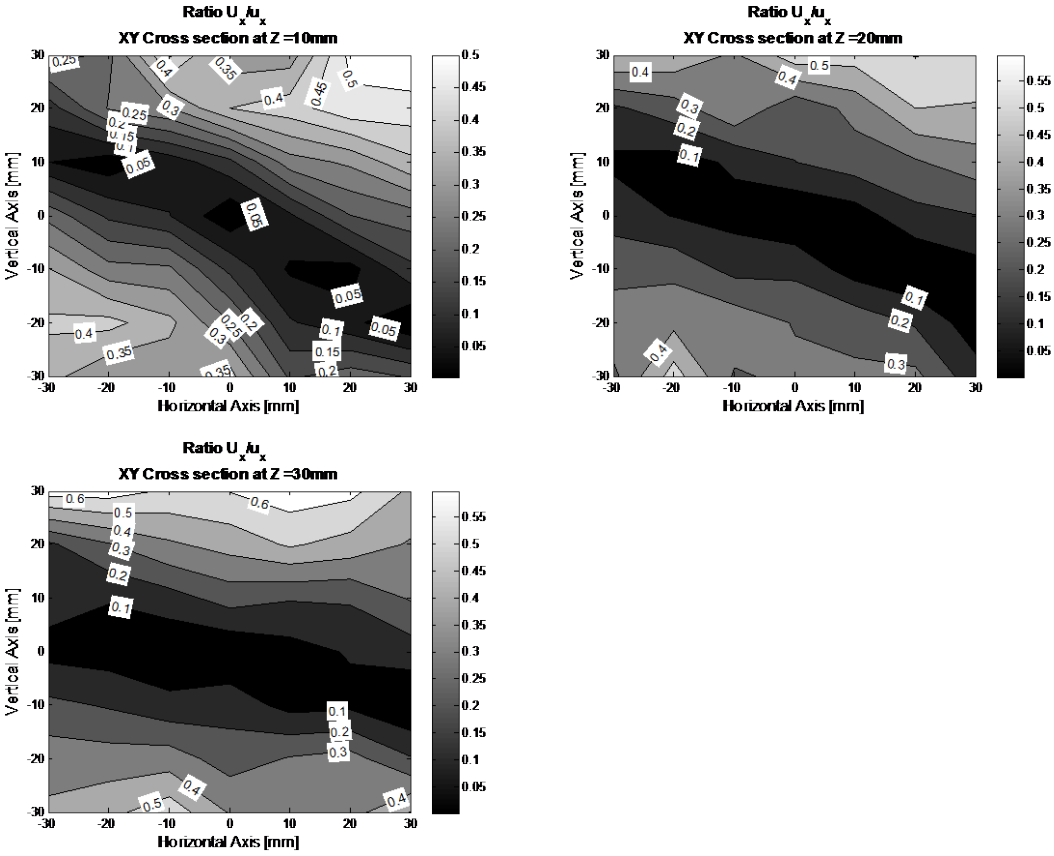

Ratio of average over fluctuation in vertical direction at 8,000 rpm

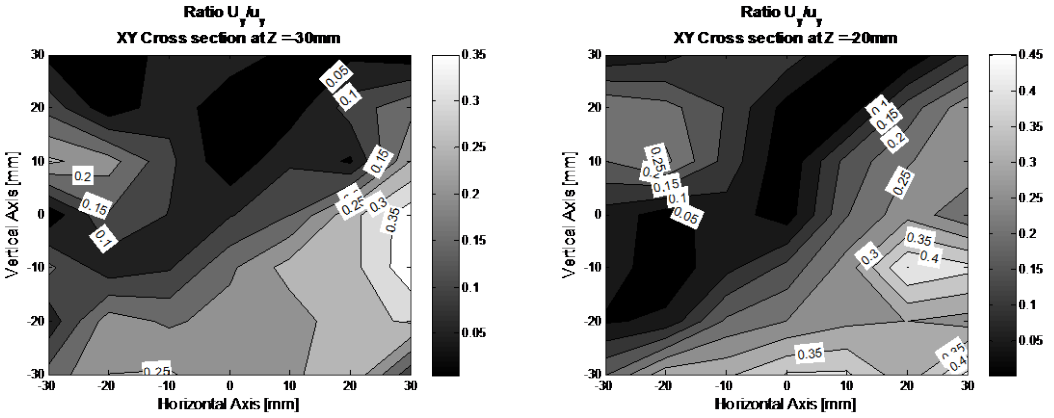

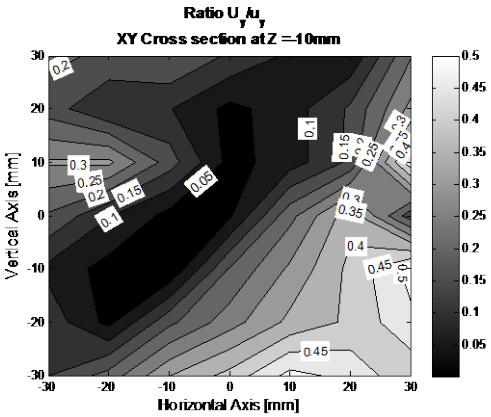
Ratio U_y/u_y
XY Cross section at Z =-10mm
Vertical Axis [mm]
Horizontal Axis [mm]

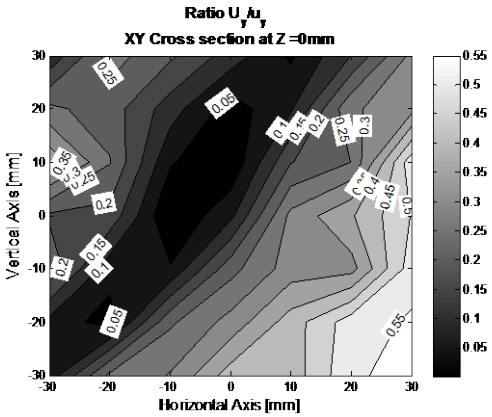
Ratio U_y/u_y
XY Cross section at Z =0mm
Vertical Axis [mm]
Horizontal Axis [mm]

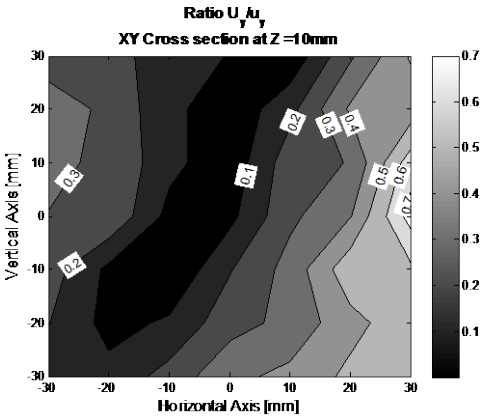
Ratio U_y/u_y
XY Cross section at Z =10mm
Vertical Axis [mm]
Horizontal Axis [mm]

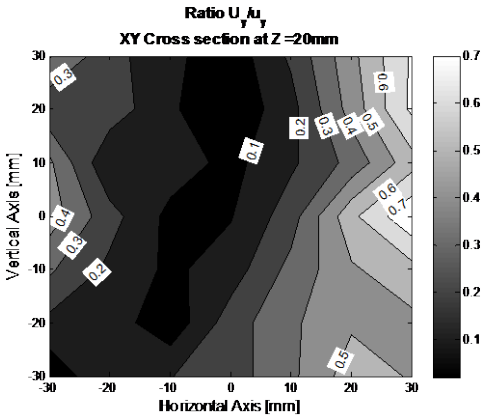
Ratio U_y/u_y
XY Cross section at Z =20mm
Vertical Axis [mm]
Horizontal Axis [mm]

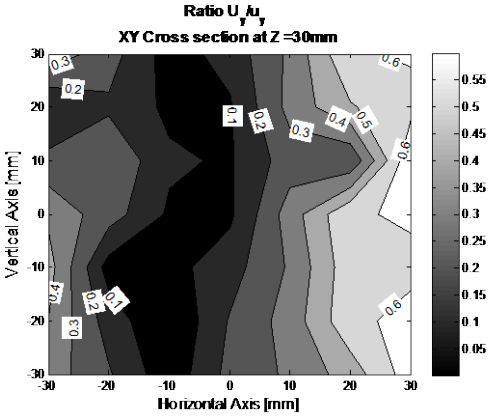
Ratio U_y/u_y
XY Cross section at Z =30mm
Vertical Axis [mm]
Horizontal Axis [mm]

Horizontal velocity Skewness at 8,000 rpm

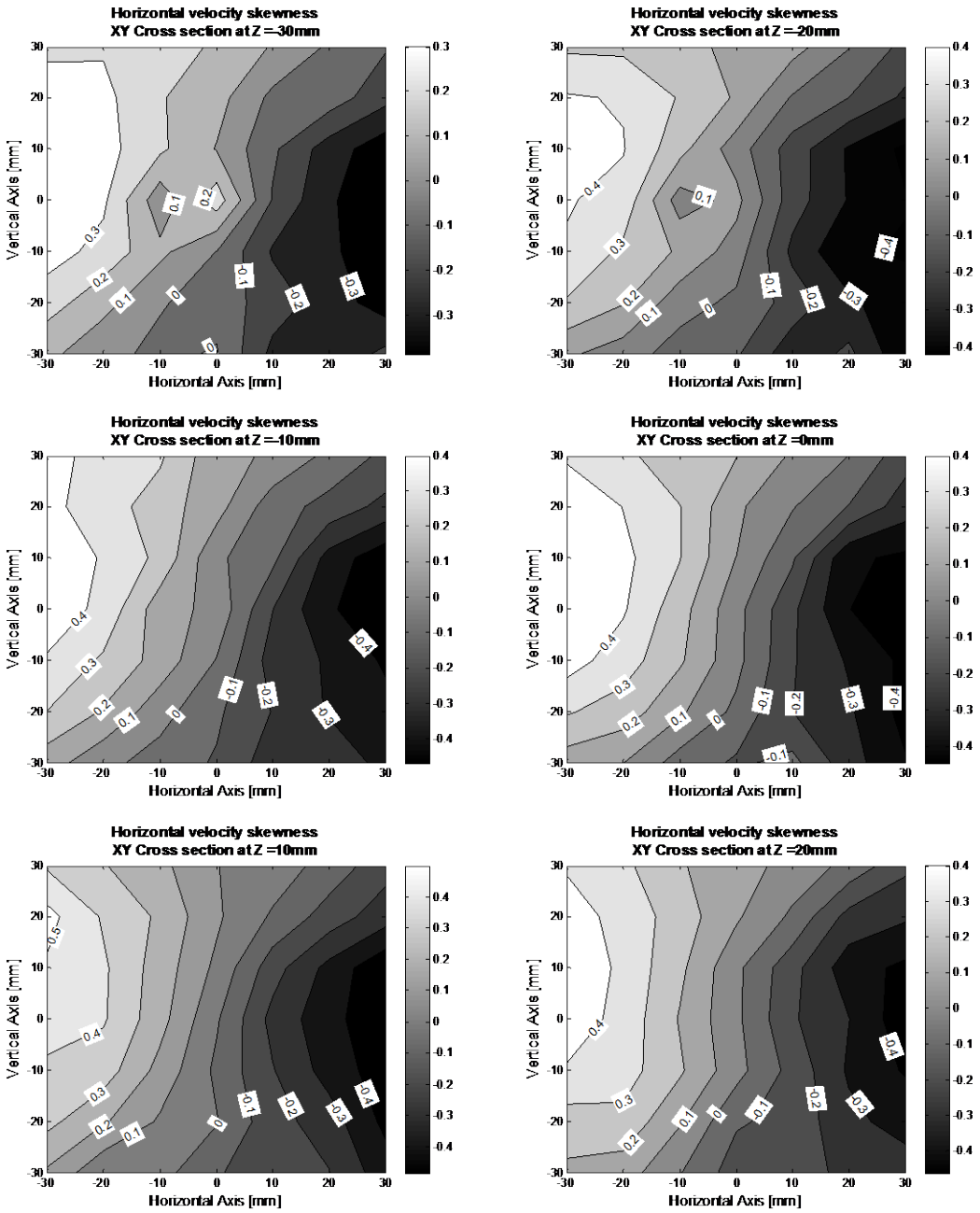

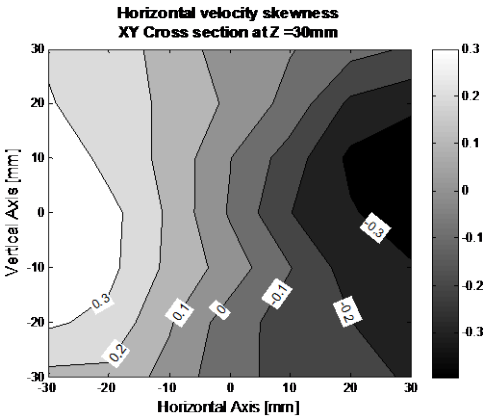

Vertical velocity Skewness at 8,000 rpm

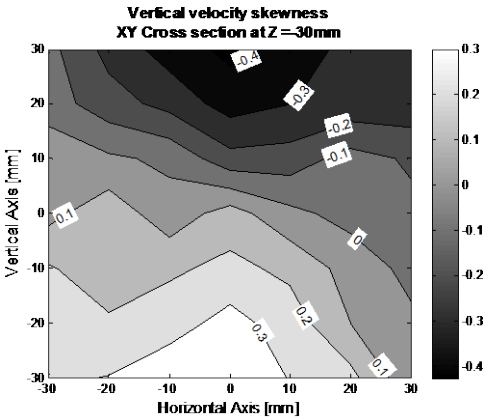

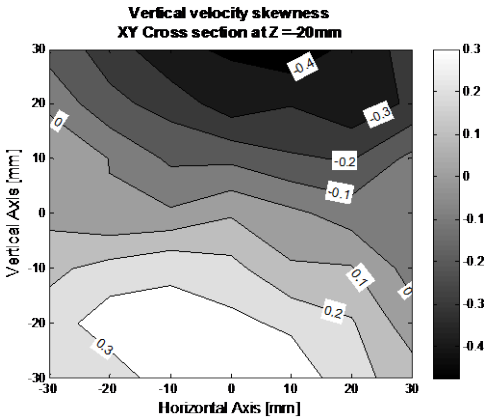

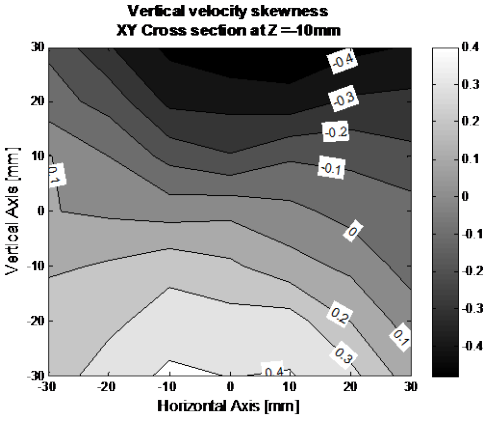

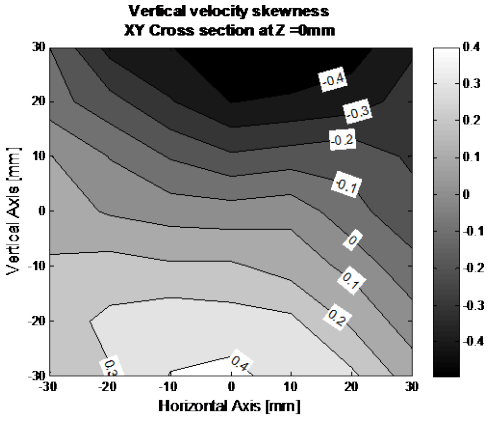

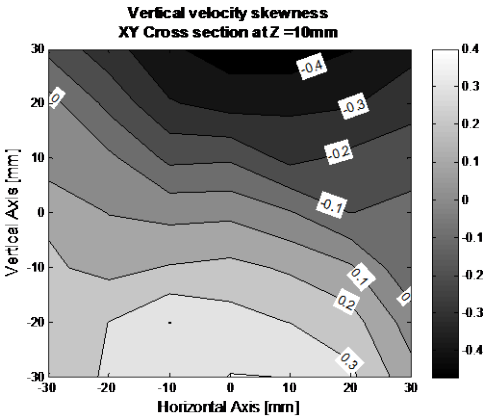

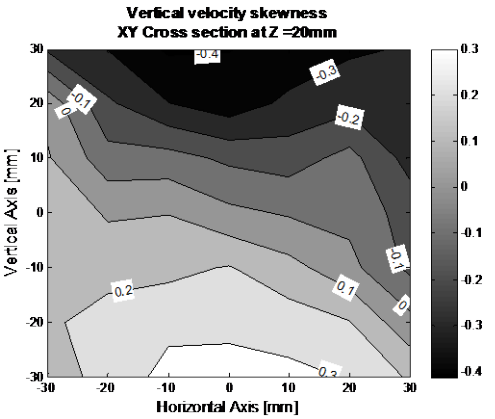

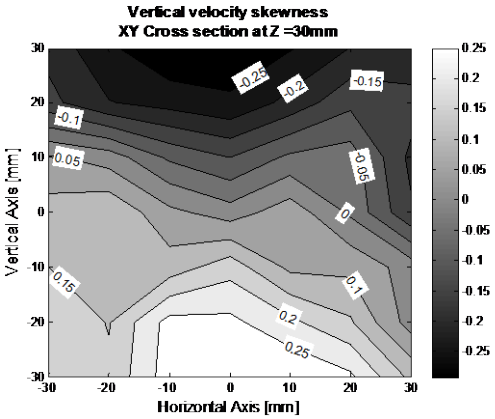

Horizontal velocity flatness at 8,000 rpm

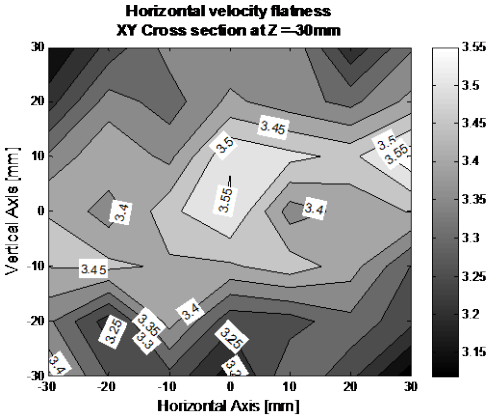

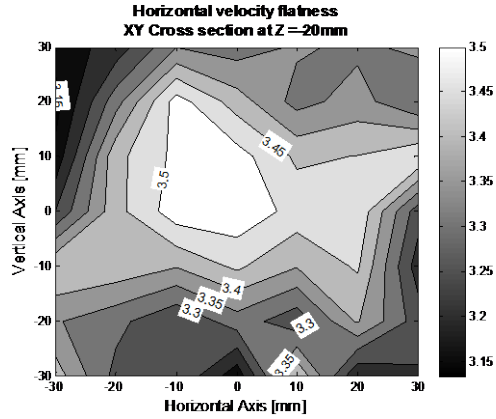

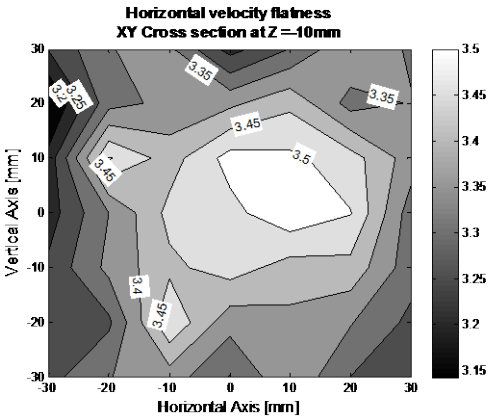
Horizontal velocity flatness
XY Cross section at Z =-10mm
Vertical Axis [mm]
Horizontal Axis [mm]

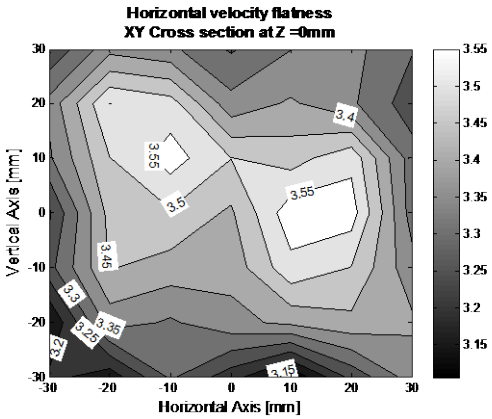
Horizontal velocity flatness
XY Cross section at Z =0mm
Vertical Axis [mm]
Horizontal Axis [mm]

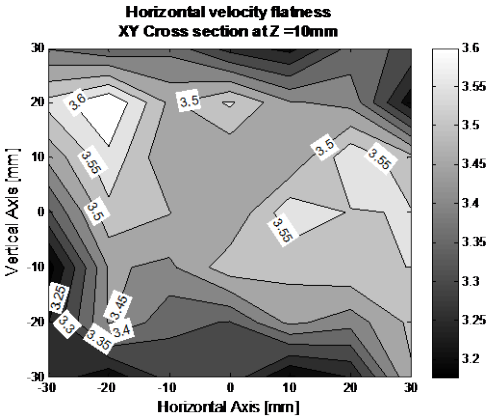
Horizontal velocity flatness
XY Cross section at Z =10mm
Vertical Axis [mm]
Horizontal Axis [mm]

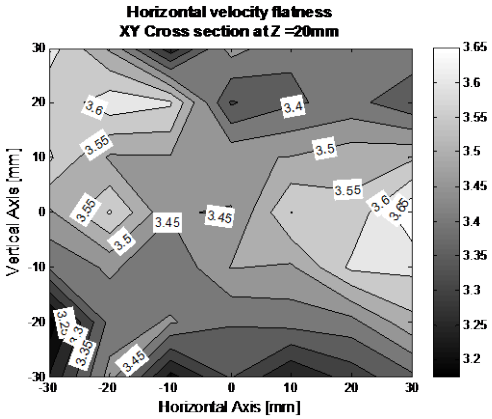
Horizontal velocity flatness
XY Cross section at Z =20mm
Vertical Axis [mm]
Horizontal Axis [mm]

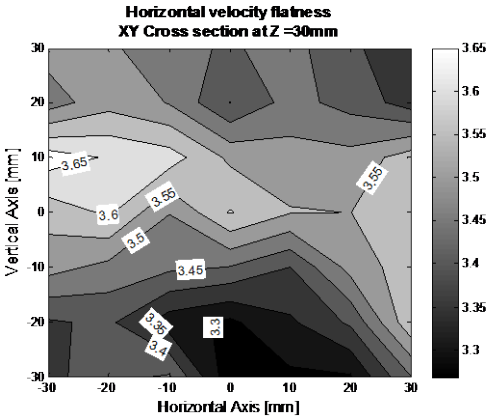
Horizontal velocity flatness
XY Cross section at Z =30mm
Vertical Axis [mm]
Horizontal Axis [mm]

Vertical velocity flatness at 8,000 rpm

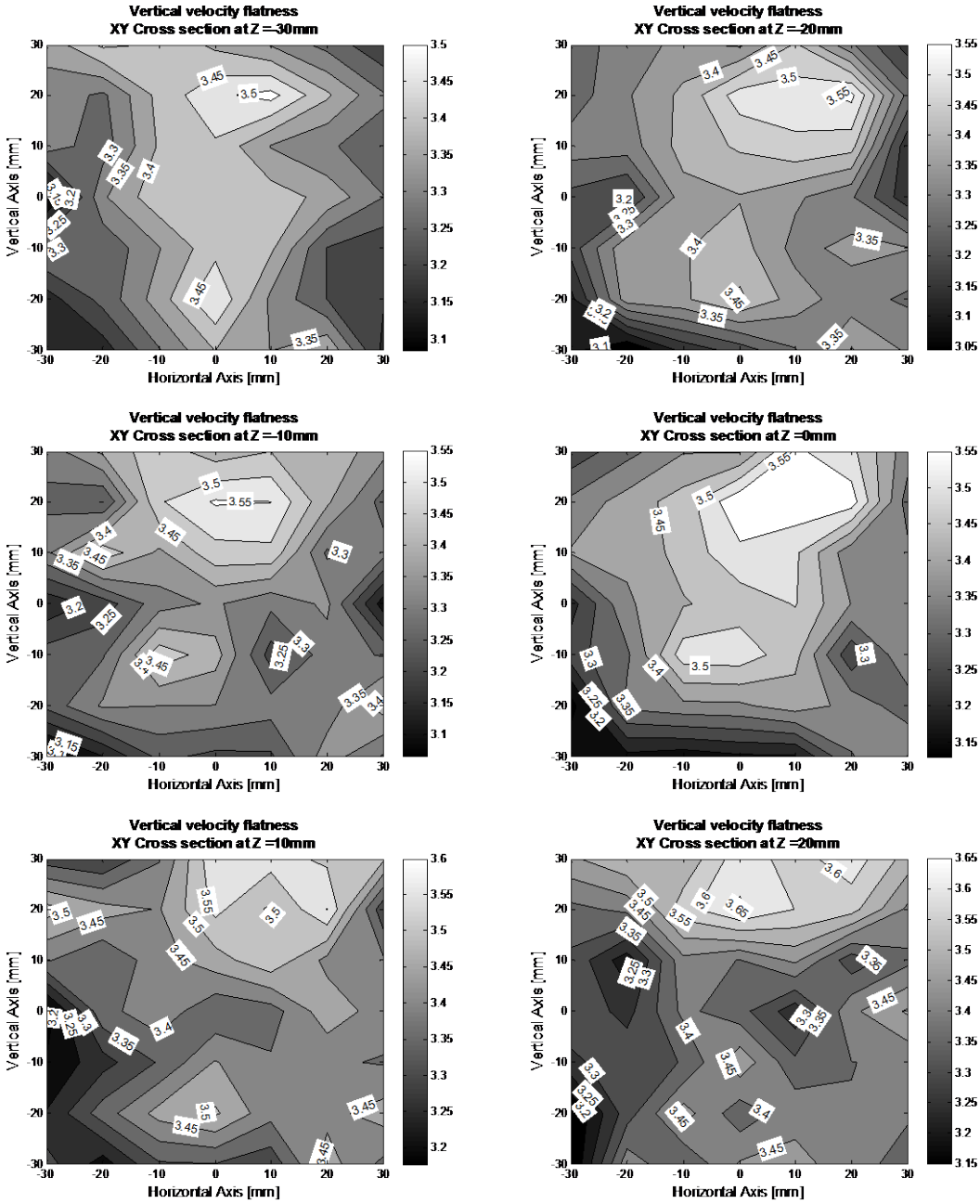

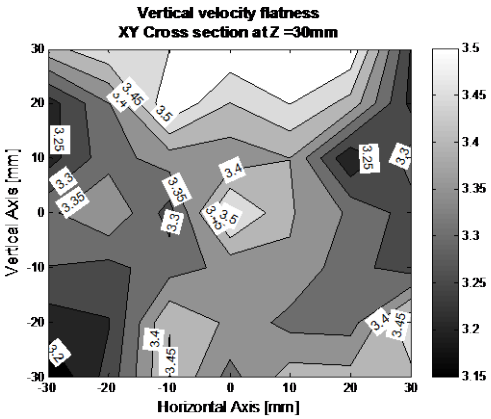

Turbulence fluctuation isotropy at 8,000 rpm

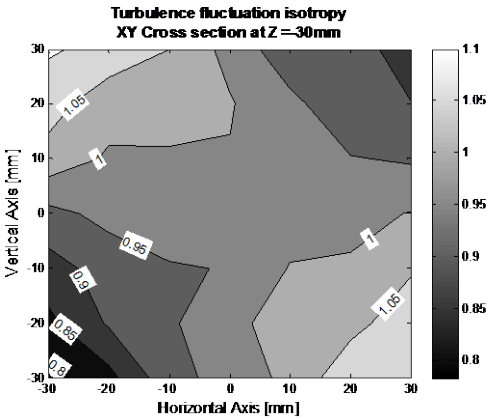

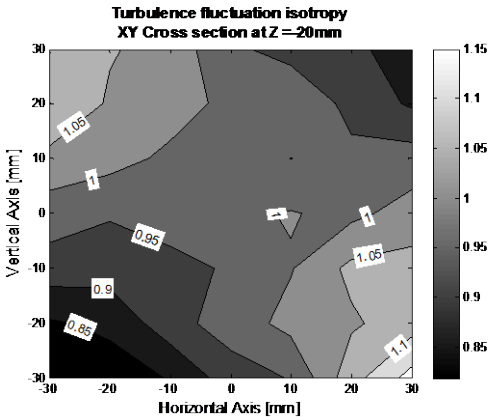

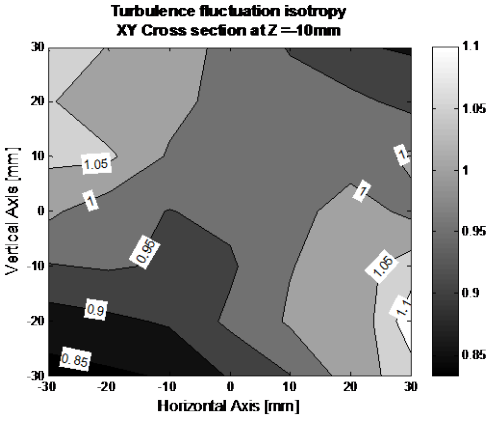

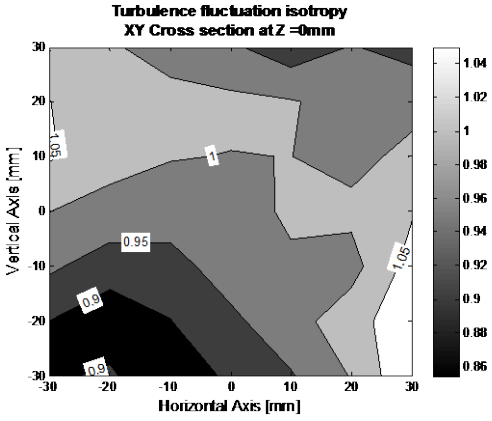

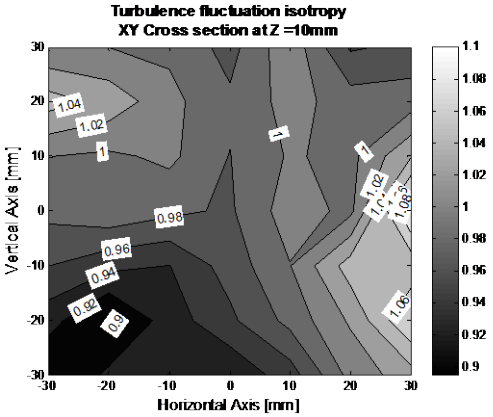

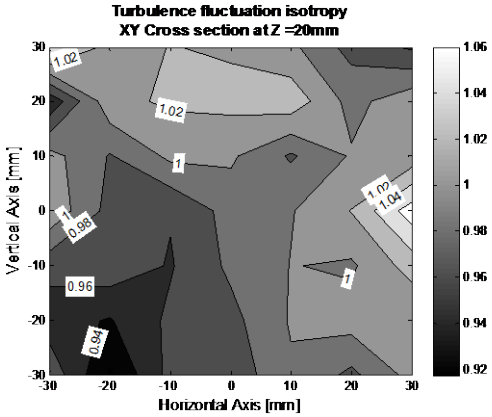

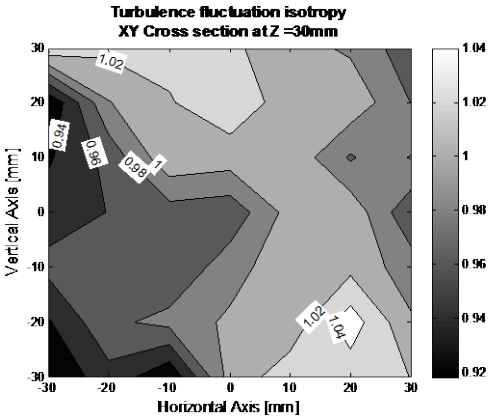

Turbulence homogeneity in the horizontal direction at 8,000 rpm

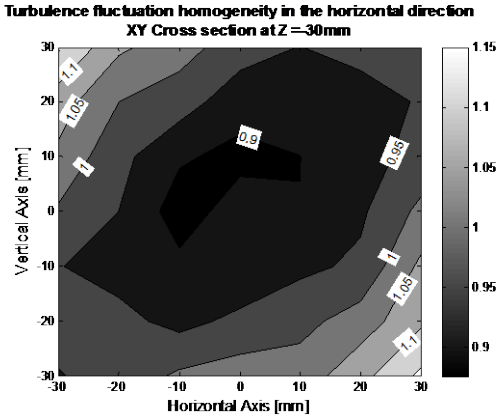

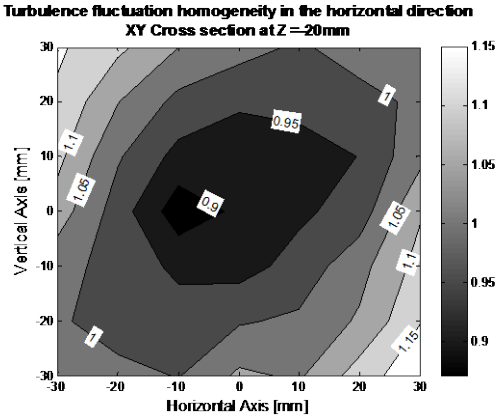

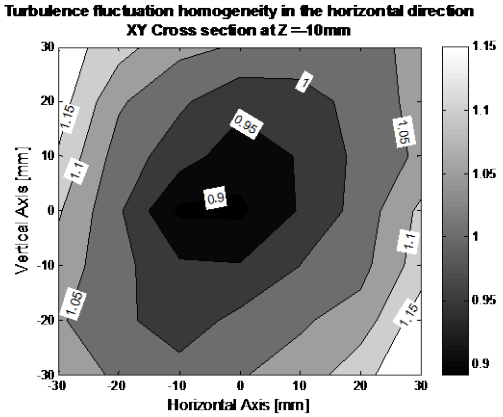
Turbulence fluctuation homogeneity in the horizontal direction
XY Cross section at Z =-10mm
Vertical Axis [mm]
Horizontal Axis [mm]

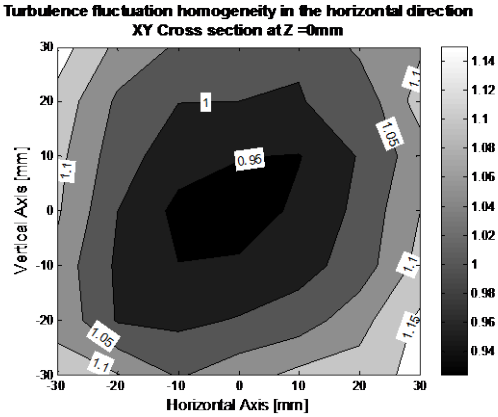
Turbulence fluctuation homogeneity in the horizontal direction
XY Cross section at Z =0mm
Vertical Axis [mm]
Horizontal Axis [mm]

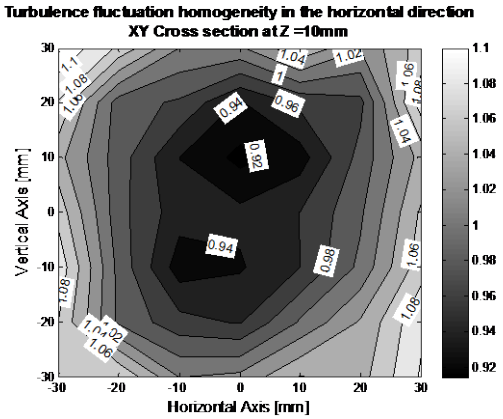
Turbulence fluctuation homogeneity in the horizontal direction
XY Cross section at Z =10mm
Vertical Axis [mm]
Horizontal Axis [mm]

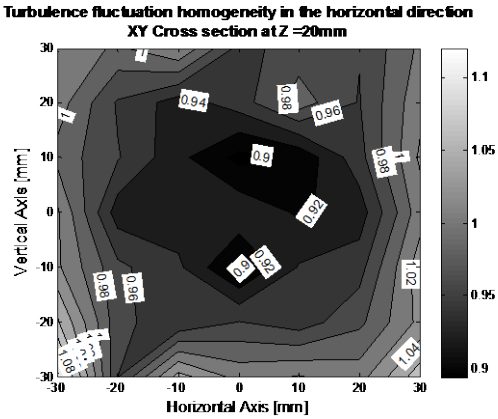
Turbulence fluctuation homogeneity in the horizontal direction
XY Cross section at Z =20mm
Vertical Axis [mm]
Horizontal Axis [mm]

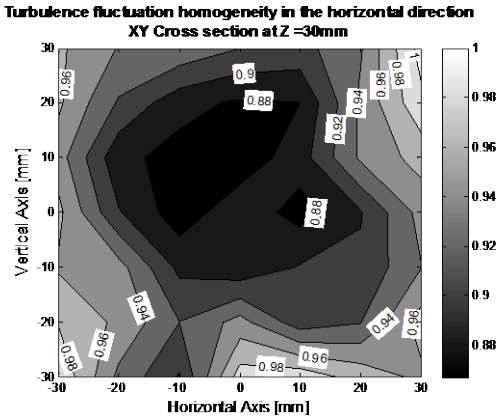
Turbulence fluctuation homogeneity in the horizontal direction
XY Cross section at Z =30mm
Vertical Axis [mm]
Horizontal Axis [mm]

Turbulence homogeneity in the vertical direction at 8,000 rpm

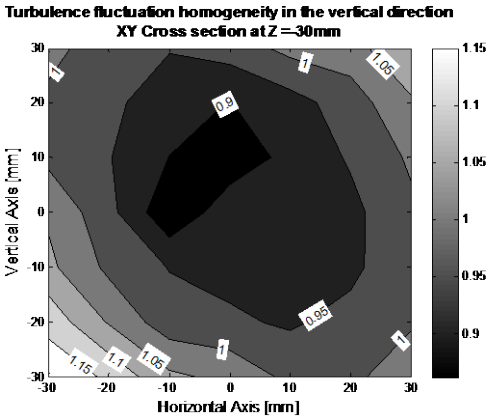

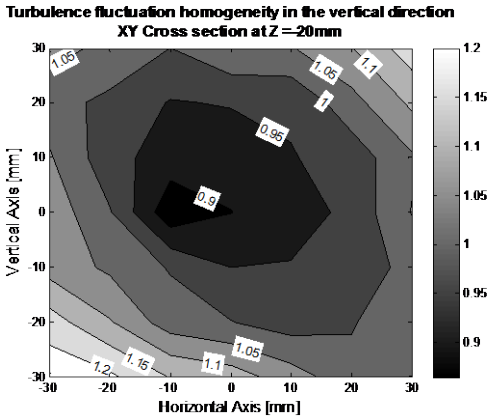

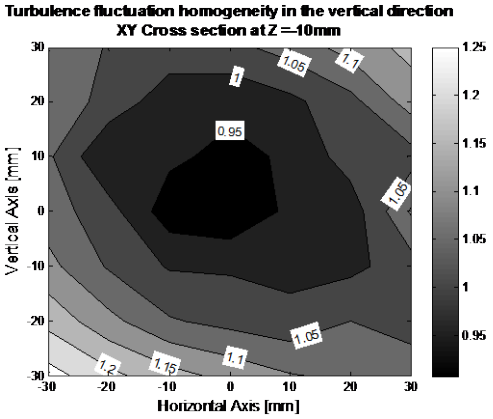

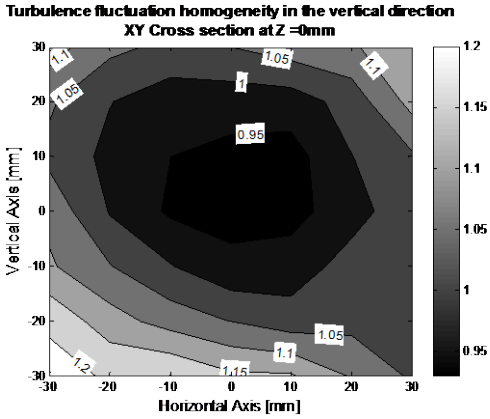

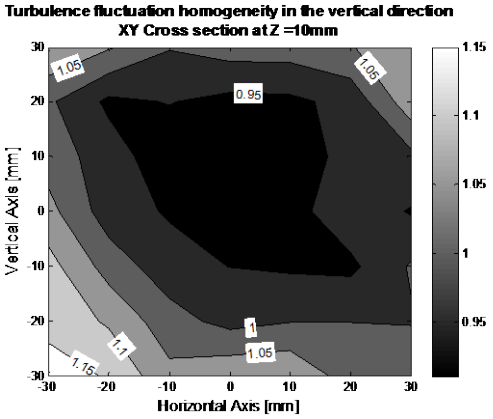

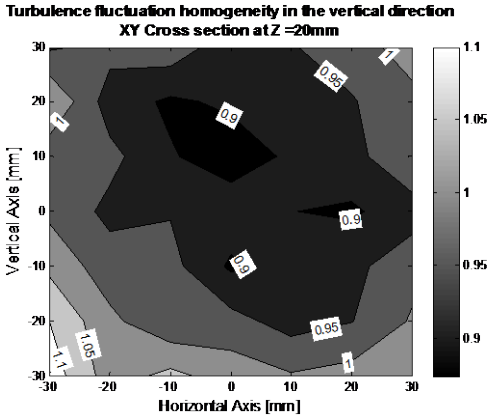

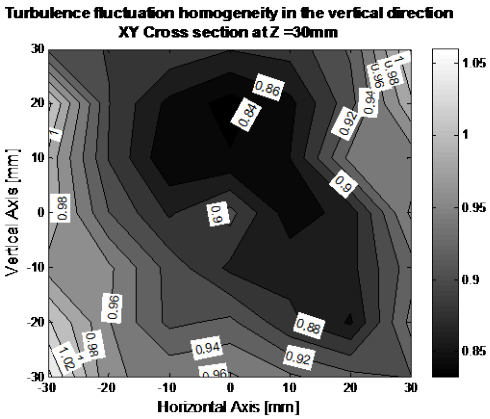

$\overline{u_x u_x}$ Reynolds stress at 8,000 rpm

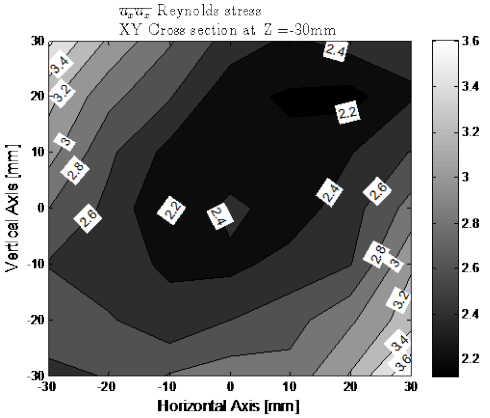

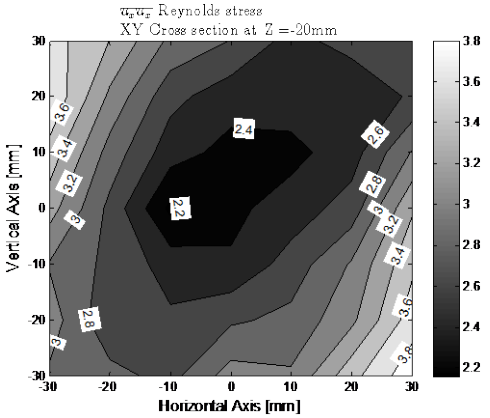

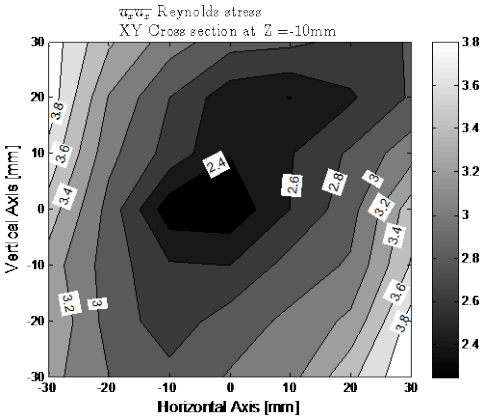

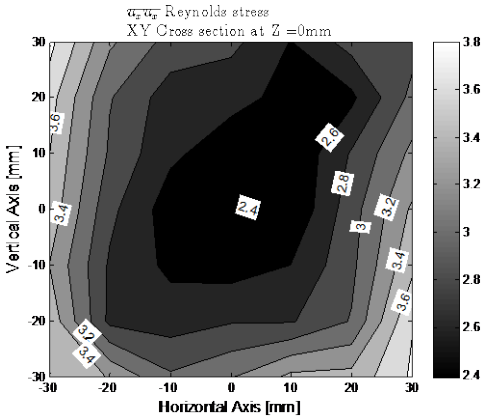

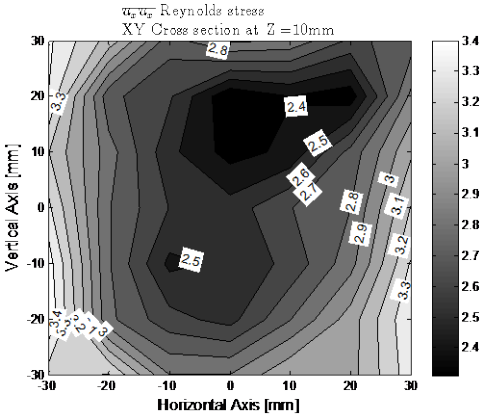

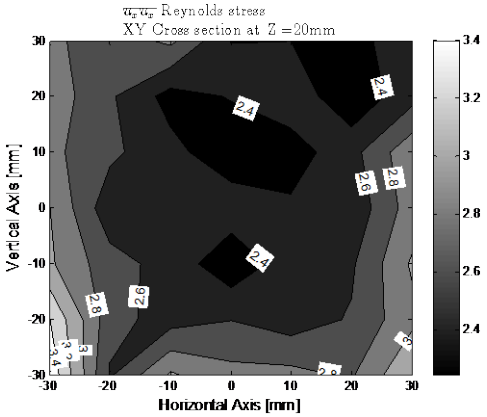

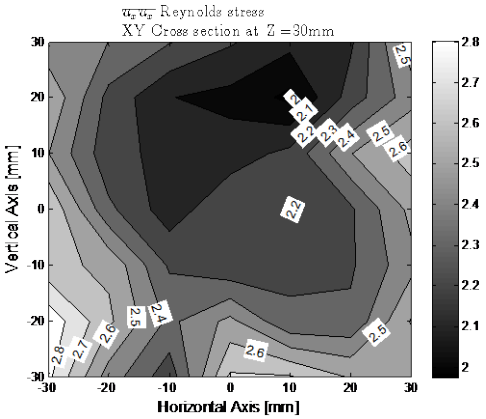

$\overline{u_y u_y}$ Reynolds stress at 8,000 rpm

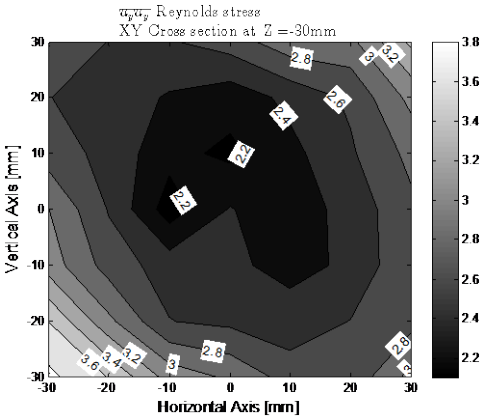

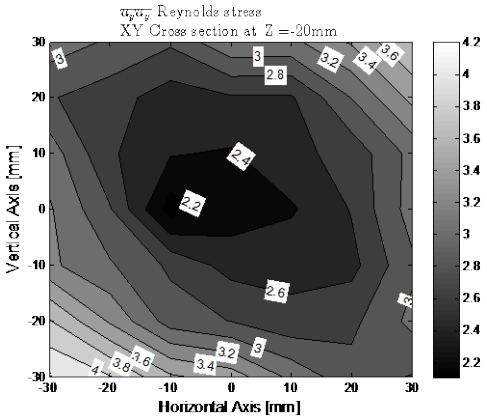

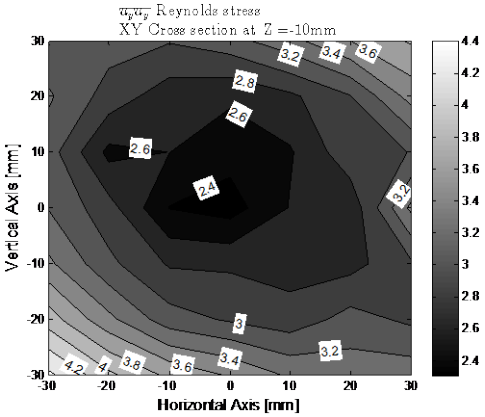
$\overline{u_y u_y}$ Reynolds stress
XY Cross section at Z =-10mm
Vertical Axis [mm]
Horizontal Axis [mm]

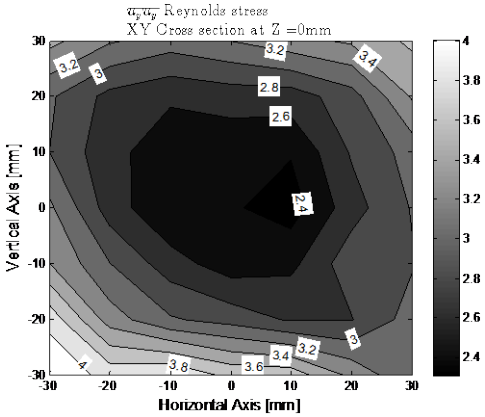
$\overline{u_y u_y}$ Reynolds stress
XY Cross section at Z =0mm
Vertical Axis [mm]
Horizontal Axis [mm]

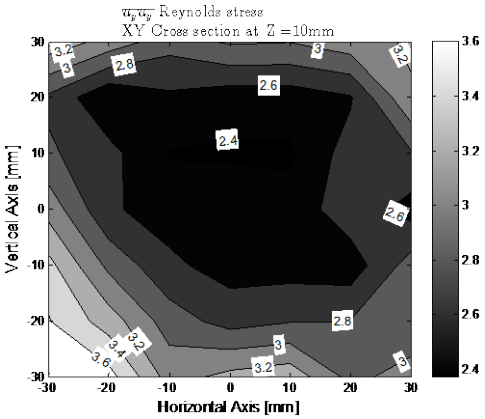
$\overline{u_y u_y}$ Reynolds stress
XY Cross section at Z =10mm
Vertical Axis [mm]
Horizontal Axis [mm]

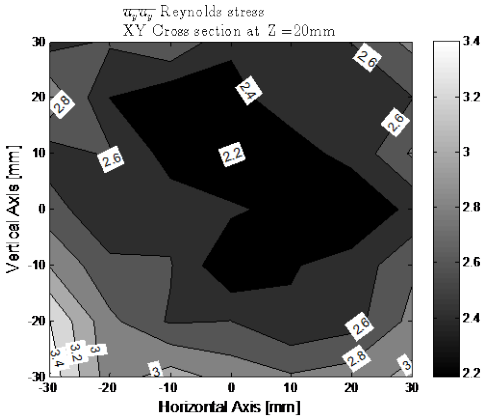
$\overline{u_y u_y}$ Reynolds stress
XY Cross section at Z =20mm
Vertical Axis [mm]
Horizontal Axis [mm]

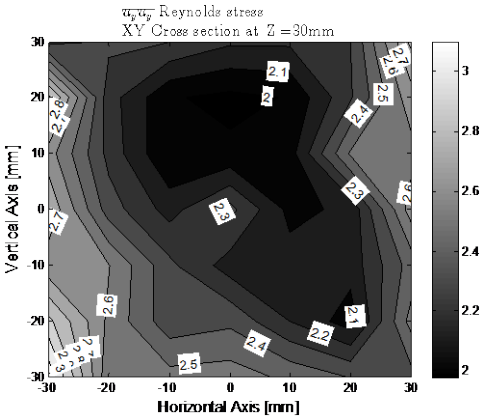
$\overline{u_y u_y}$ Reynolds stress
XY Cross section at Z =30mm
Vertical Axis [mm]
Horizontal Axis [mm]

$\overline{u_x u_y}$ Reynolds stress at 8,000 rpm

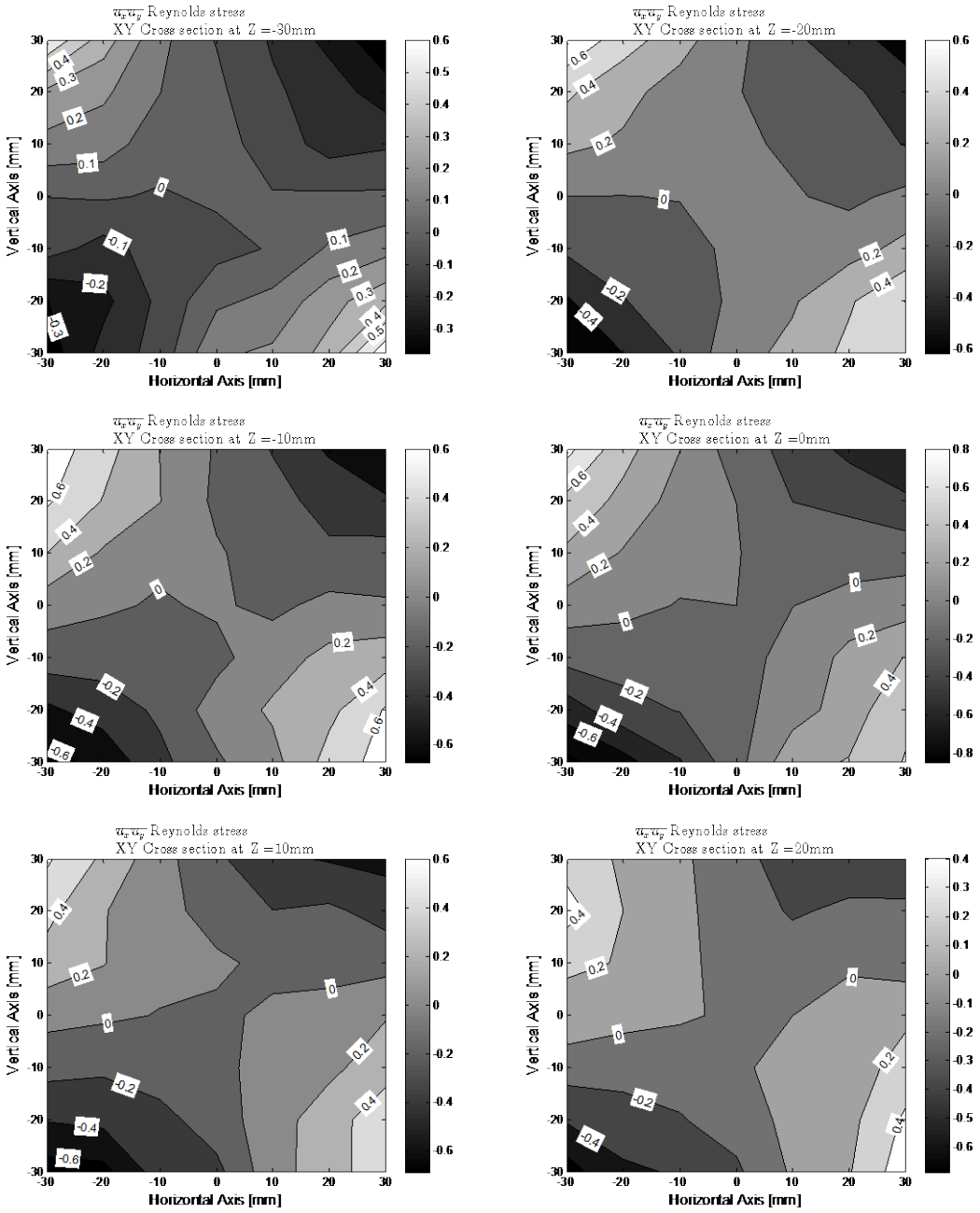

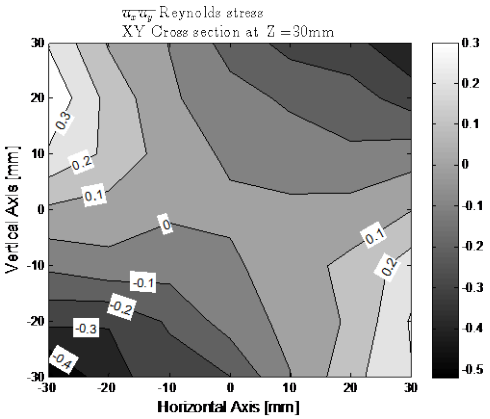

Vector plot at 8,000 rpm

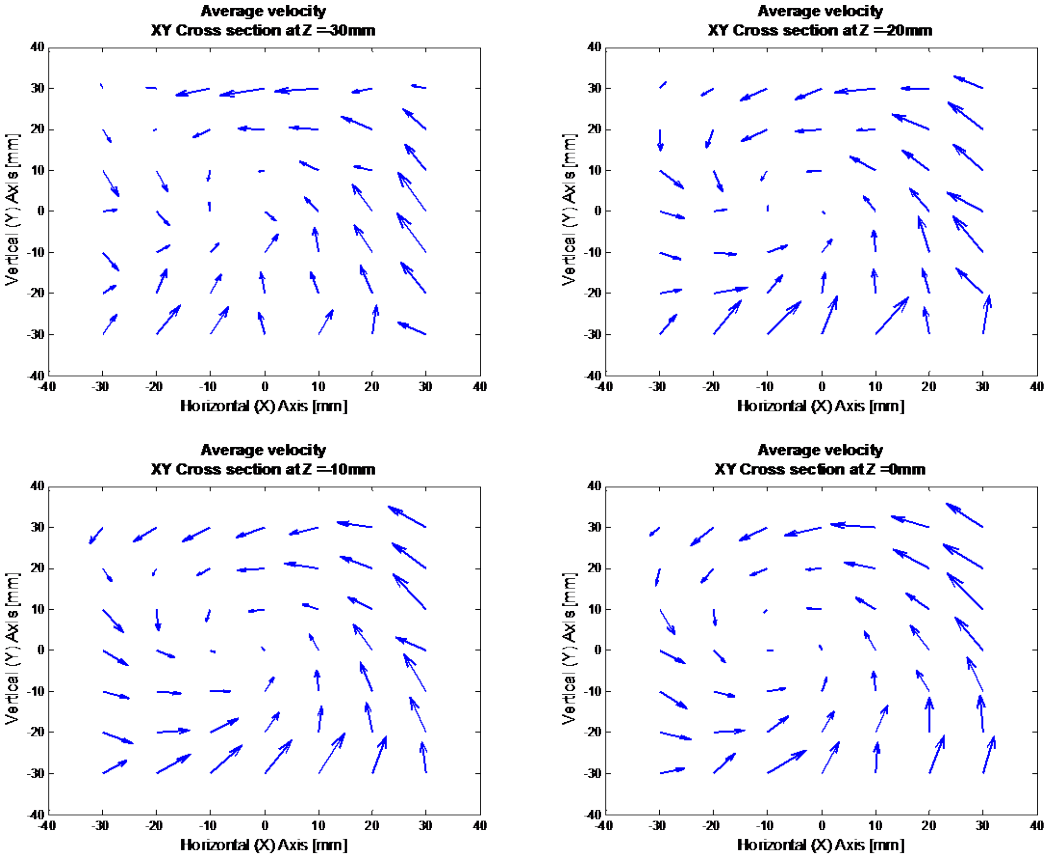

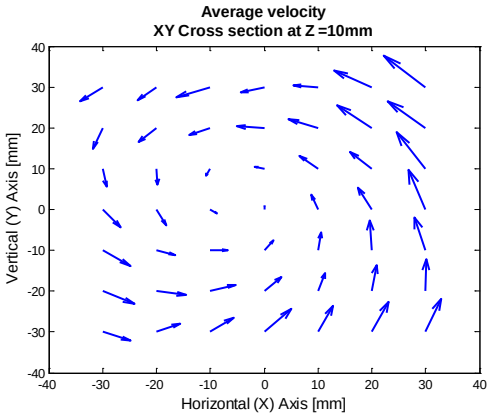

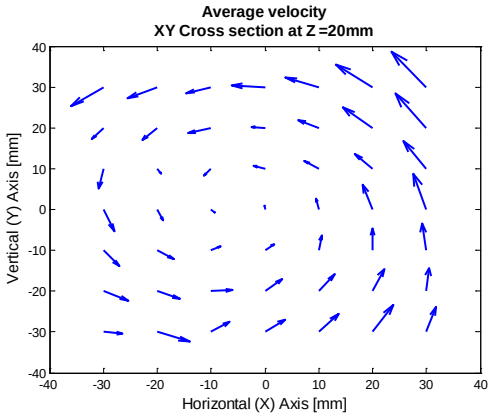

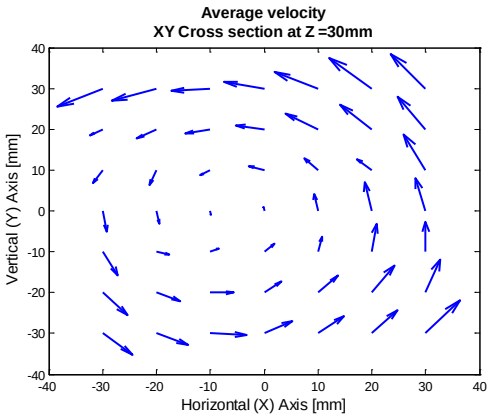

Streamlines at 8,000 rpm

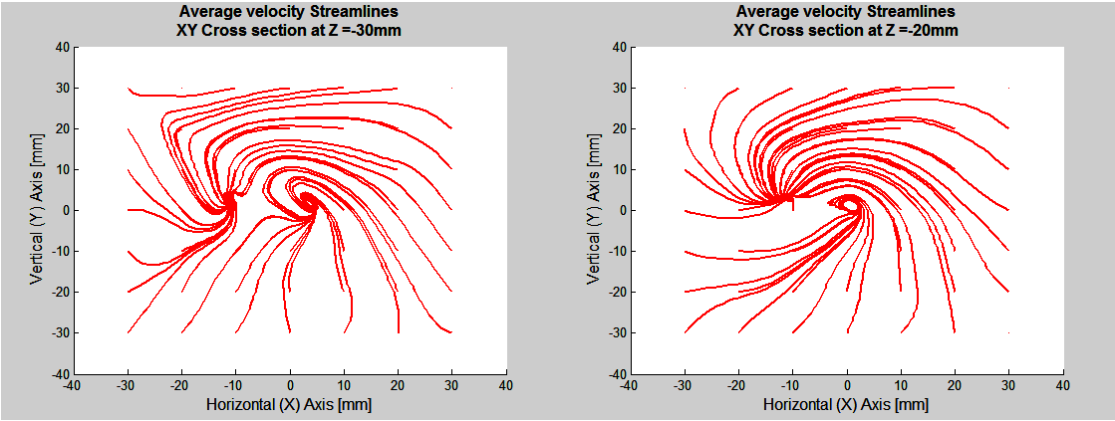

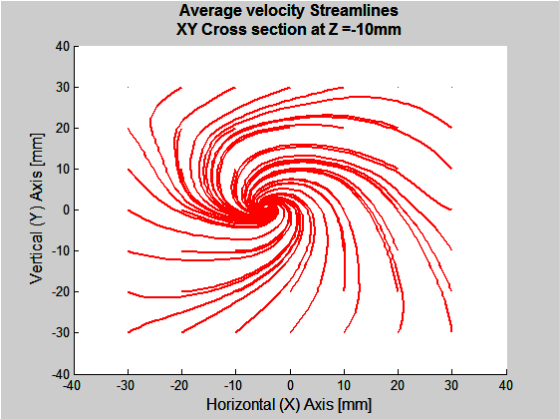
Average velocity Streamlines
XY Cross section at Z =-10mm
Vertical (Y) Axis [mm]
Horizontal (X) Axis [mm]

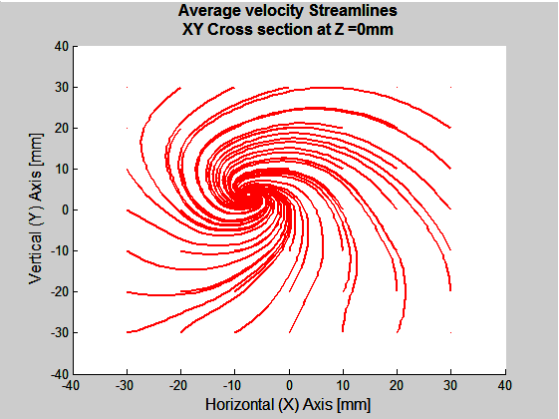
Average velocity Streamlines
XY Cross section at Z =0mm
Vertical (Y) Axis [mm]
Horizontal (X) Axis [mm]

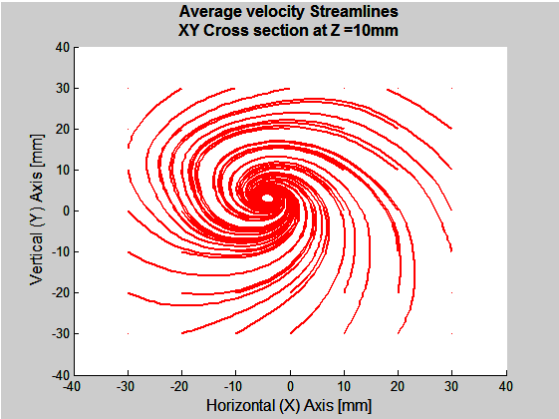
Average velocity Streamlines
XY Cross section at Z =10mm
Vertical (Y) Axis [mm]
Horizontal (X) Axis [mm]

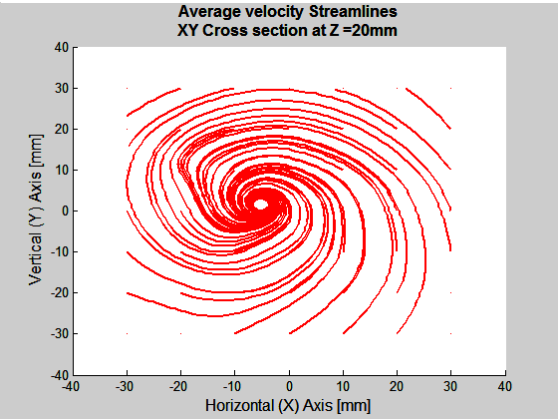
Average velocity Streamlines
XY Cross section at Z =20mm
Vertical (Y) Axis [mm]
Horizontal (X) Axis [mm]

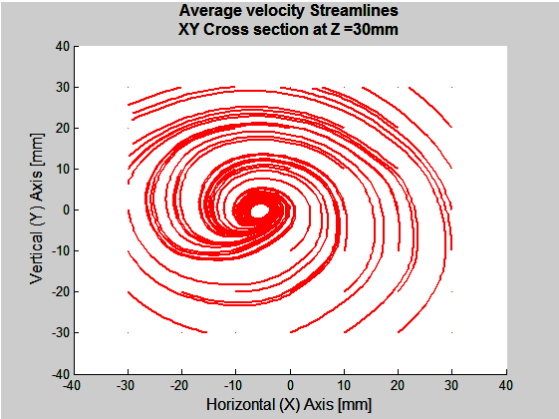
Average velocity Streamlines
XY Cross section at Z =30mm
Vertical (Y) Axis [mm]
Horizontal (X) Axis [mm]

APPENDIX B

PLOTS OF MEASUREMENTS AT 12,000 RPM

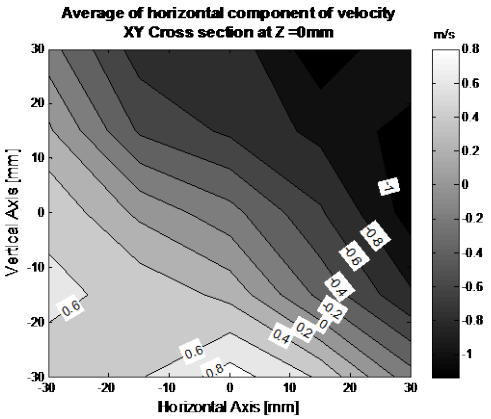

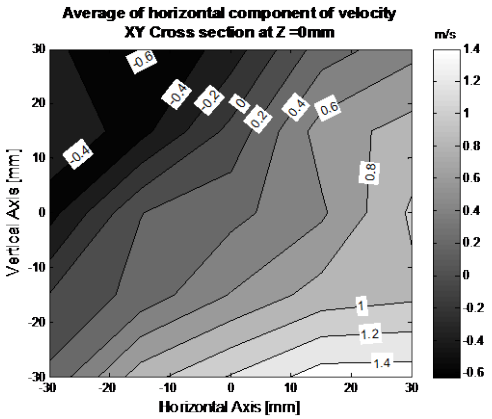

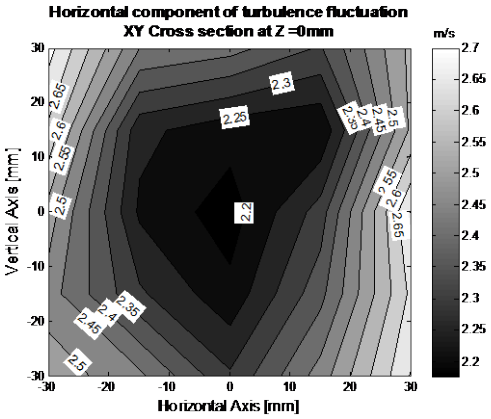

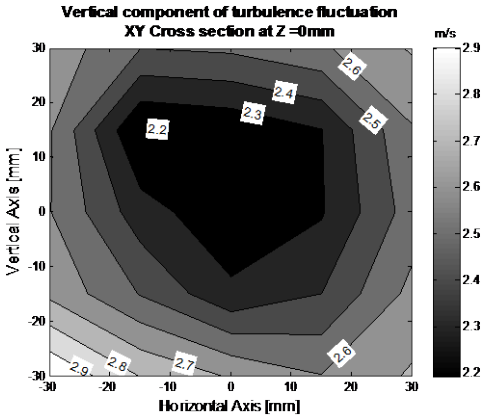

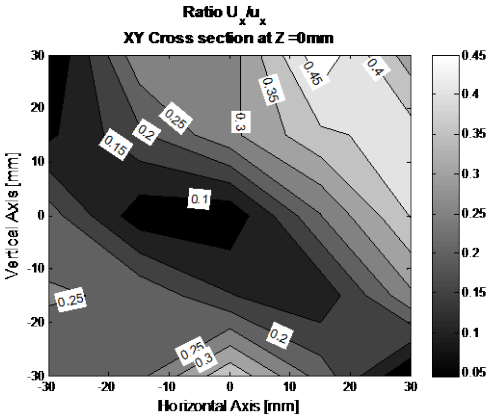

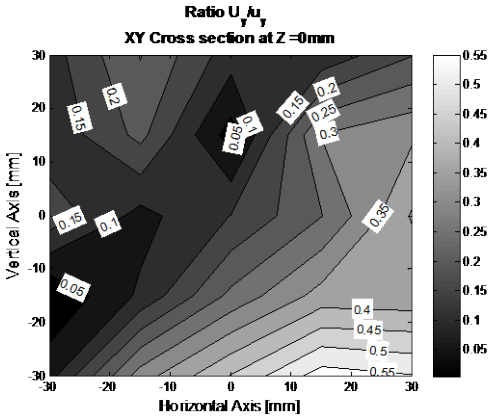

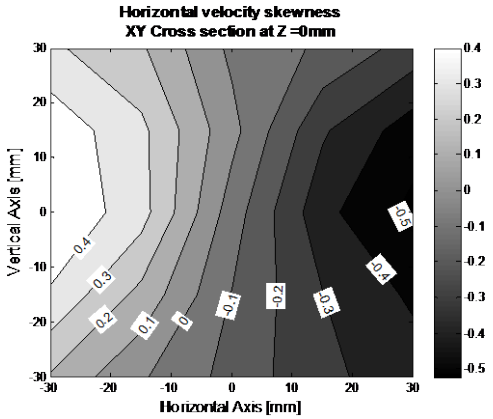
Horizontal velocity skewness
XY Cross section at Z =0mm
Vertical Axis [mm]
Horizontal Axis [mm]

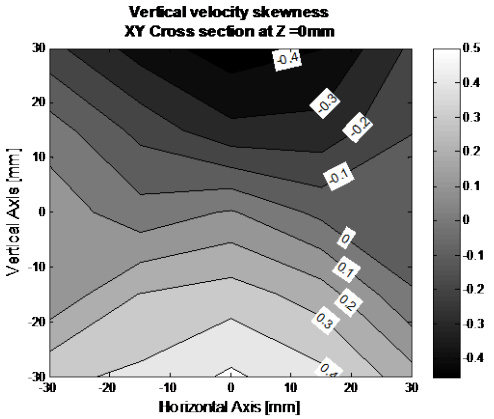
Vertical velocity skewness
XY Cross section at Z =0mm
Vertical Axis [mm]
Horizontal Axis [mm]

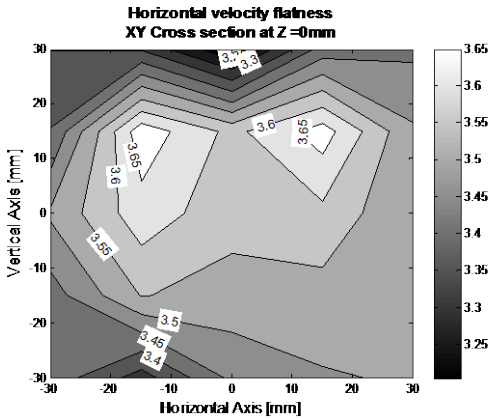
Horizontal velocity flatness
XY Cross section at Z =0mm
Vertical Axis [mm]
Horizontal Axis [mm]

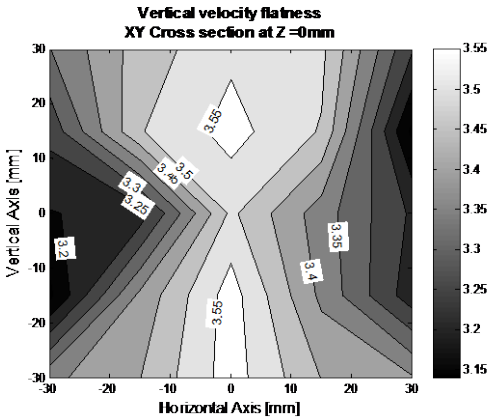
Vertical velocity flatness
XY Cross section at Z =0mm
Vertical Axis [mm]
Horizontal Axis [mm]

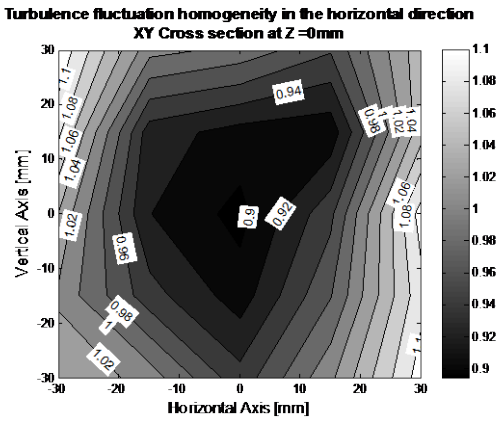
Turbulence fluctuation homogeneity in the horizontal direction
XY Cross section at Z =0mm
Vertical Axis [mm]
Horizontal Axis [mm]

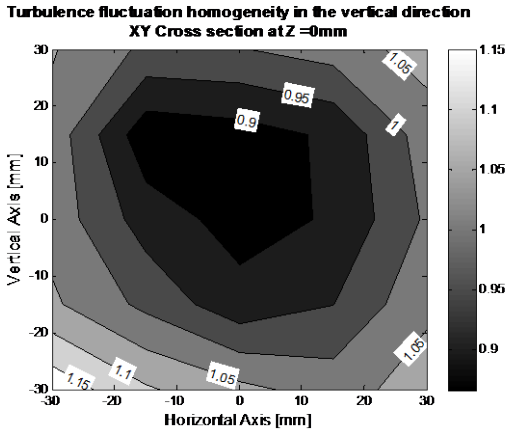
Turbulence fluctuation homogeneity in the vertical direction
XY Cross section at Z =0mm
Vertical Axis [mm]
Horizontal Axis [mm]

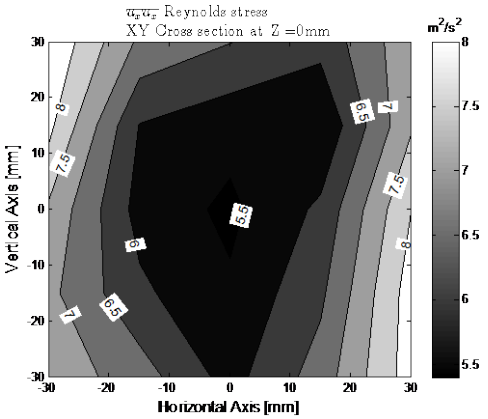
$\overline{u_x u_x}$ Reynolds stress
XY Cross section at Z =0mm
m²/s²
Vertical Axis [mm]
Horizontal Axis [mm]

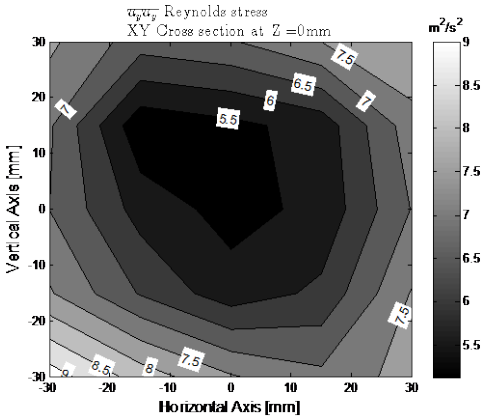
$\overline{u_y u_y}$ Reynolds stress
XY Cross section at Z =0mm
m²/s²
Vertical Axis [mm]
Horizontal Axis [mm]

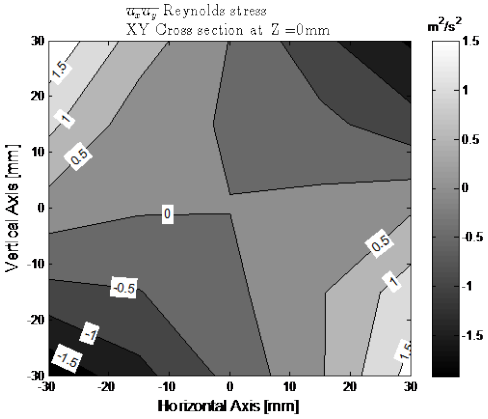
$\overline{u_x u_y}$ Reynolds stress
XY Cross section at Z =0mm
m²/s²
Vertical Axis [mm]
Horizontal Axis [mm]

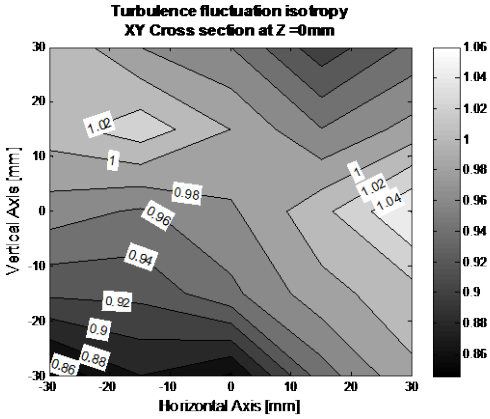
Turbulence fluctuation isotropy
XY Cross section at Z =0mm
Vertical Axis [mm]
Horizontal Axis [mm]

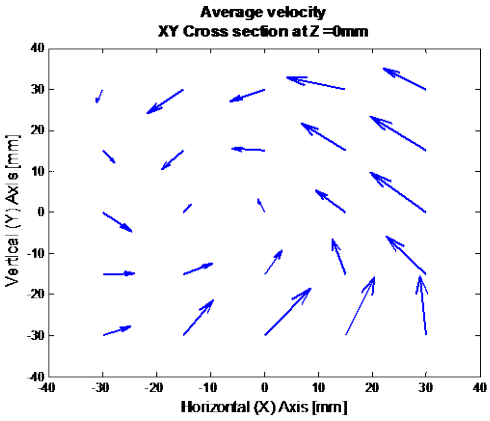
Average velocity
XY Cross section at Z =0mm
Vertical (Y) Axis [mm]
Horizontal (X) Axis [mm]

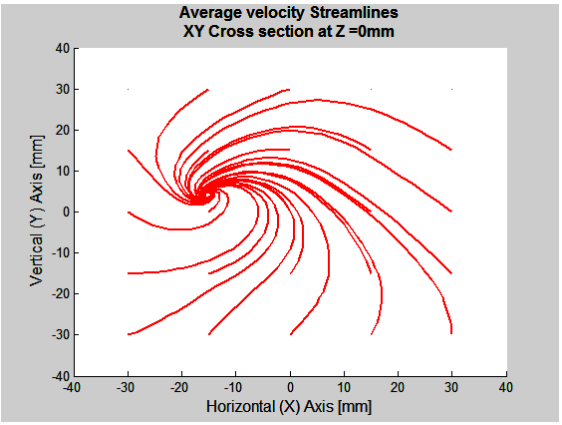
Average velocity Streamlines
XY Cross section at Z =0mm
Vertical (Y) Axis [mm]
Horizontal (X) Axis [mm]

APPENDIX C

SUMMARY OF UNCORRECTED RESULTS (BIASED)

Parameter		Formula	8,000 rpm		12,000	
			$i = x$	$i = y$	$i = x$	$i = y$
Average velocity	m/s	$U_i(\mathbf{x})$	0.06	0.09	0.01	0.20
Turbulence fluctuation	m/s	$u_{i,rms}(\mathbf{x})$	1.67	1.67	2.59	2.61
Axial average velocity	m/s	$U_z(\mathbf{x})$	0.51		1.58	
Ratio average/fluctuation		$\|U_i(\mathbf{x})\| / u_{i,rms}(\mathbf{x})$	0.22	0.25	0.25	0.22
Skewness		$\frac{1}{N}\sum_{n=1}^{N}(u_i(t_n;\mathbf{x}))^3 \Big/ \left(u_{i,rms}\right)^3$	0.02	0.02	-0.02	0.03
Flatness		$\frac{1}{N}\sum_{n=1}^{N}(u_i(t_n;\mathbf{x}))^4 \Big/ \left(u_{i,rms}\right)^4$	3.48	3.42	3.49	3.39
Turbulence isotropy		$u_{x,rms}(\mathbf{x}) / u_{y,rms}(\mathbf{x})$	1.00		1.00	
Turbulence homogeneity		$u_{i,rms}(\mathbf{x}) / \overline{u_{i,rms}}$	1.00	1.00	1.00	1.00
Normal Reynold stress	m^2/s^2	$\overline{u_i(\mathbf{x})u_i(\mathbf{x})}$	2.80	2.81	6.77	6.86
Shear Reynolds stress	m^2/s^2	$\overline{u_x(\mathbf{x})u_y(\mathbf{x})}$	-0.01		0.01	

APPENDIX D

LESSONS LEARNED

Clogged jet in particle generator

A small piece of debris found its way into the jet orifice, in the particle generator. The symptom was a drastic loss in the data rate and the number of acquired samples per run. The amount of the data was not reproducible in locations that were scanned previously with identical experimental settings.

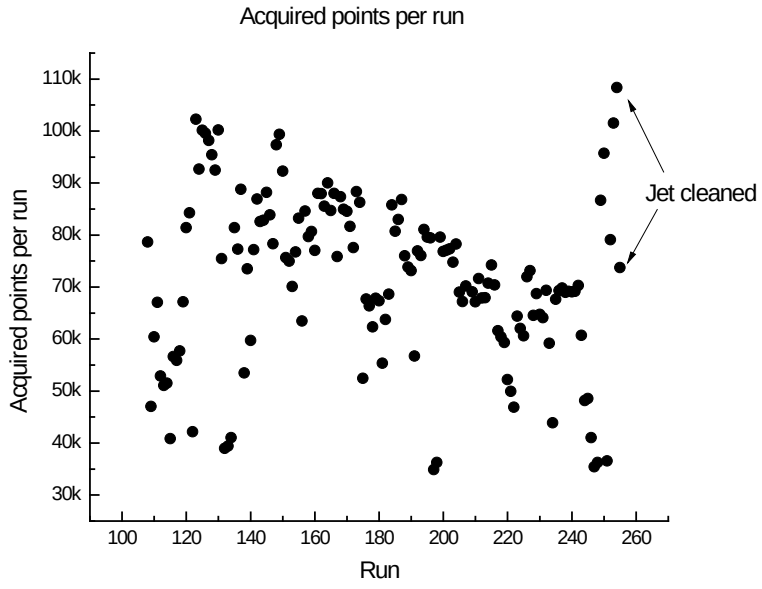

Drop in number of points acquired per run. The data rate recovered after the particle generator was cleaned

The seed generator was opened for inspection, and pieces of a broken plastic plug were found in the deposit and in one of the jet orifices. Lesson learned: verify the particle generator prior to taking measurements.

Debris particle generator deposit

Small particle in jet orifice.

Reflections

When properly aligned, the reflections of the LDV beams from the bomb window will bounce back to the LDV probe. The reflections are much more powerful than the weak scattered light and the noise overwhelms signal. Lesson learned: block reflections and keep windows clean.

Seeding

The seeding has to be controlled. Too much seeding and the particles scatter the incoming laser beams before they reach the probe volume and also scattered the burst light. Too few seeds in the bomb and the data rate is low. A maximum was found in the data rate by timing the particle generator operation. The best results were obtained with

simultaneous three jets working for 4 seconds prior to a run. The life of the particles is time sensitive, so there was little wait for run start after the particle injection.

The vessel had to be cleared of seed after each run and then freshly reseeded prior to a new run. This procedure was done with a regular vacuum cleaner. Lower data rates were observed if no particle were added, i.e. particle recycling, see figure below. Addition of fresh particles to “old” particles remaining from a previous run also gave poor results.

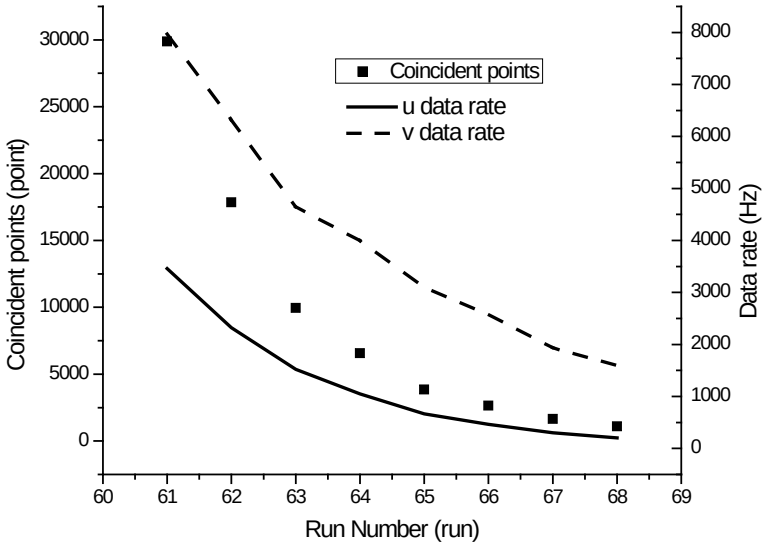

The runs performed back to back with no particle replenishing. Notice the drop in number of data points.